ARL-TR-9998 • OCT 2024

# Field Validation of Two Boundary Layer Optical Turbulence Models over Desert Surfaces

by Sean G O'Brien, Jeffrey O Johnson, and Gordon A MacDonald

ARL-TR-9998 • OCT 2024

# Field Validation of Two Boundary Layer Optical Turbulence Models over Desert Surfaces

**by Sean G O'Brien and Jeffrey O Johnson**
*DEVCOM Army Research Laboratory*

**Gordon A MacDonald**
*Bennett Aerospace, Inc.*

# REPORT DOCUMENTATION PAGE

| 1. REPORT DATE | 2. REPORT TYPE | 3. DATES COVERED START DATE | END DATE |
|---|---|---|---|
| October 2024 | Technical Report | October 2021 | November 2023 |

**4. TITLE AND SUBTITLE**
Field Validation of Two Boundary Layer Optical Turbulence Models over Desert Surfaces

| 5a. CONTRACT NUMBER | 5b. GRANT NUMBER | 5c. PROGRAM ELEMENT NUMBER |
|---|---|---|
| **5d. PROJECT NUMBER** | **5e. TASK NUMBER** | **5f. WORK UNIT NUMBER** |

**6. AUTHOR(S)**
Sean G O'Brien, Jeffrey O Johnson, and Gordon A MacDonald

| 7. PERFORMING ORGANIZATION NAME(S) AND ADDRESS(ES) | 8. PERFORMING ORGANIZATION REPORT NUMBER |
|---|---|
| DEVCOM Army Research Laboratory<br>ATTN: FCDD-RLA-ID<br>White Sands Missile Range, NM 88002 | ARL-TR-9998 |

| 9. SPONSORING/MONITORING AGENCY NAME(S) AND ADDRESS(ES) | 10. SPONSOR/MONITOR'S ACRONYM(S) | 11. SPONSOR/MONITOR'S REPORT NUMBER(S) |
|---|---|---|
| | | |

**12. DISTRIBUTION/AVAILABILITY STATEMENT**
DISTRIBUTION STATEMENT A. Approved for public release: distribution is unlimited.

**13. SUPPLEMENTARY NOTES**
Primary author's email: <sean.g.obrien.civ@army.mil>.

**14. ABSTRACT**
The plan and preliminary results for a comparison of two methods for computing optical turbulence strength $C_n^2$ at a near-surface reference level are presented. Both methods use measurements of wind speed, temperature, air pressure, and specific humidity at two closely spaced levels in the atmospheric surface layer to determine the Monin–Obukhov length at the reference level and to then determine the value of $C_n^2$ through similarity theory. The two-level approach lends itself to rapid field evaluation of optical turbulence vertical profiles in the surface layer that are critical for estimation of scintillation and beam wander effects in free-space optical communication and high-energy laser propagation models.

**15. SUBJECT TERMS** optical turbulence, boundary layer, Meteorological Sensor Array, NAVSLaM, TurbZr, WSMR, Electromagnetic Spectrum Sciences; Military Information Sciences

| 16. SECURITY CLASSIFICATION OF: a. REPORT | b. ABSTRACT | C. THIS PAGE | 17. LIMITATION OF ABSTRACT | 18. NUMBER OF PAGES |
|---|---|---|---|---|
| UNCLASSIFIED | UNCLASSIFIED | UNCLASSIFIED | SAR | 62 |

| 19a. NAME OF RESPONSIBLE PERSON | 19b. PHONE NUMBER *(Include area code)* |
|---|---|
| Sean G O'Brien | 575-678-1570 |

**STANDARD FORM 298 (REV. 5/2020)**
*Prescribed by ANSI Std. Z39.18*

## Contents

## List of Figures

## List of Tables

## Acknowledgments

The authors wish to sincerely thank Mr Robert Brice, Mr Sean D'Arcy, Mr Jeffrey Swanson, and Mr Edward Creegan of DEVCOM Army Research Laboratory (ARL) and Mr Erick Reynoso and Mr Mark Spychala of the New Mexico State University's Physical Science Laboratory for their skilled implementation of hardware and software that were essential to the success of this project. They have provided expert support at critical points in this task under frequently difficult weather and field conditions. The authors would also like to thank Dr Christopher Hocut of ARL for his insightful technical advice and management of ARL personnel from his team.

# 1. Introduction

## 1.1 Rationale

A field experiment was designed to compare the performance of a two-level version of the Navy Atmospheric Vertical Surface Layer Model (NAVSLaM), Version 2.0 MATLAB code,[1,2] and TurbZr, a Java-based extension of the US Army Combat Capabilities Development Command (DEVCOM) Army Research Laboratory (ARL) MARIAH model[3,4] for calculation of boundary layer optical turbulence strength ${C_n}^2$ at land-based locations. Both of these models use gradients of temperature, pressure, wind speed, and specific humidity from meteorological tower measurements at two levels in the atmospheric surface layer, providing an estimate of ${C_n}^2$ at a reference level close to the surface.

The **NA**VSLaM/**Tur**bZr **E**valuation experiment (NATurE), as this field study is called, will provide needed validation of the two-level NAVSLaM model over desert terrain and will examine the validity of the MARIAH approach to estimating the Monin–Obukhov (MO) scaling length from two-level meteorological data. In addition, the use of sonic anemometers to estimate optical turbulence strength will also be evaluated from the same data set. The validating comparison standards are long and short path scintillometer measurements of diurnal optical turbulence strength variations over baselines close to selected Meteorological Sensor Array (MSA) meteorological towers.

The test configuration employed meteorological sensors in the central core of ARL's MSA and scintillometers to provide nearly co-located estimates of ${C_n}^2$ via three basic independent approaches:

1. Direct scintillometer measurements near the MSA towers
2. Model estimates based on measurements collected at two levels on the MSA towers
3. Quasi-point measurements reduced from MSA tower sonic data

This report is concerned only with the first two methods. A follow-up report will address comparisons of optical turbulence scintillometer measurement data with values derived from sonic anemometer measurements.

## 1.2 Background

A brief review is provided for the algorithms and design of the two models that are compared in this test. These codes estimate optical turbulence strength at specific reference levels in the boundary layer from near-surface meteorological parameter gradients. A reduction algorithm that estimates optical turbulence strength from sonic anemometer measurements is also briefly discussed.

## 1.3 NAVSLaM

The NAVSLaM for optical turbulence analysis was developed primarily for marine boundary layer environments in the 0–100 m above sea level (ASL) altitude region. A recent adaptation of this model (NAVSLaM 2.0) to terrestrial environments has been developed that uses standard meteorological parameter inputs (air temperature, wind speed, and relative humidity) measured at two near-surface levels. NAVSLaM's performance over sea surfaces has been extensively studied, but efforts to validate the two-level terrestrial version have only recently appeared in the literature.[5] Relevant implementation details for the two-level NAVSLaM model (as extracted from the MATLAB source code) are summarized in the following discussion. NAVSLaM uses an iterative approach to calculate MO scaling law parameters from a two-level meteorological measurement. Initial values for these parameters are estimated from the following relations:

$$u_{*o} = \frac{(u_2 - u_1)k}{\log(z_{u2}/z_{u1})} \tag{1}$$

$$T_{*o} = \frac{(\theta_2 - \theta_1)k}{\log(z_{T2}/z_{T1})} \tag{2}$$

$$q_{*o} = \frac{(q_2 - q_1)k}{\log(z_{h2}/z_{h1})} \tag{3}$$

$$T_{*v} = T_{*o}(1 + \gamma\,\bar{q}) + \gamma\,\bar{T}\,q_{*o} \tag{4}$$

$$L_o = \frac{\bar{\theta_v}\,u_{*o}^2}{k\,g\,T_{*v}}, \tag{5}$$

where $u_2, u_1$ are the wind speeds (m/s) measured at levels $z_{u2}$ and $z_{u1}$ (m) above ground level (AGL), $\theta_2, \theta_1$ are the potential temperatures (K) at $z_{T2}$, and $z_{T1}$, $q_2, q_1$ are the specific humidities (g/g) at $z_{h2}$ and $z_{h1}$. The von Karmann constant is given by $k = 0.4$, $\gamma \approx 0.622$ is the molecular weight ratio of water vapor to dry air, and $g$ is the local gravitational constant (m/s$^2$). The averaged quantities are given by $\bar{q} = (q_2 + q_1)/2$, $\bar{T} = (T_2 + T_1)/2$, and $\bar{\theta_v} = (\theta_{v2} + \theta_{v1})/2$. Here, $T_2, T_1$ are the absolute temperatures (K), and $\theta_{v2}, \theta_{v1}$ are the virtual potential temperatures ($\theta_v = \theta(1 + \gamma\, q)$) at levels $z_{T2}$ and $z_{T1}$, respectively. $L_o$ is the initial guess of the MO scaling length.

These initial values are then iterated over index $i$ using the relations:

$$u_{*i} = \frac{(u_2 - u_1)k}{\log(z_{u2}/z_{u1})} - \psi_m(z_{u2}/L_{i-1}) + \psi_m(z_{u1}/L_{i-1}) \tag{6}$$

$$T_{*i} = \frac{(\theta_2 - \theta_1)k}{\log(z_{T2}/z_{T1})} - \psi_T(z_{T2}/L_{i-1}) + \psi_T(z_{T1}/L_{i-1}) \tag{7}$$

$$q_{*i} = \frac{(q_2 - q_1)k}{\log(z_{h2}/z_{h1})} - \psi_T(z_{h2}/L_{i-1}) + \psi_T(z_{h1}/L_{i-1}) \tag{8}$$

$$T_{*v} = T_{*i}(1 + \gamma\, \bar{q}) + \gamma\, \bar{T}\, q_{*i} \tag{9}$$

$$L_i = \frac{\bar{\theta_v}\, u_{*i}^2}{k\, g\, T_{*v}} \tag{10}$$

The wind speed profile function $\psi_m(\zeta)$ is given by

$$\psi_m(\zeta) = 2\ln((1 + x)/2) + \ln((1 + x^2)/2) - 2\arctan(x) + \pi/2 \tag{11}$$

$$x = (1 - 16\zeta)^{1/4} \tag{12}$$

for unstable $(\zeta < 0)$ conditions. For stable $(\zeta > 0)$ conditions, $\psi_m(\zeta)$ is given by

$$
\begin{aligned}
\psi_m(\zeta) =& \frac{-3a_m}{b_m}(x-1) + \frac{a_m B_m}{2b_m}\left[2\ln\frac{x+B_m}{1+B_m} - \ln\frac{x^2 - B_m x + B_m^2}{1 - B_m + B_m^2}\right] \\
&+ \frac{\sqrt{3}a_m B_m}{b_m}\left[\arctan\frac{2x - B_m}{\sqrt{3}B_m} - \arctan\frac{2 - B_m}{\sqrt{3}B_m}\right]
\end{aligned}
\tag{13}
$$

$$
x = (1+\zeta)^{1/3}, \tag{14}
$$

where

$$
a_m = 5, \qquad b_m = 5/6.5, \qquad B_m = ((1-b_m)/b_m)^{1/3} \tag{15}
$$

The potential temperature profile function $\psi_T(\zeta)$ is given by

$$
\psi_T(\zeta) = 2\ln((1+x)/2) \tag{16}
$$

$$
x = (1-16\zeta)^{1/2} \tag{17}
$$

for unstable $(\zeta < 0)$ conditions. For stable $(\zeta > 0)$ situations, $\psi_T(\zeta)$ assumes the form

$$
\psi_T(\zeta) = -\frac{b_h}{2}\ln(1 + c_h\zeta + \zeta^2) + (-\frac{a_h}{B_h} + \frac{b_h c_h}{2B_h})\left[\ln\frac{2\zeta + c_h - B_h}{2\zeta + c_h + B_h} - \ln\frac{c_h - B_h}{c_h + B_h}\right], \tag{18}
$$

where

$$
a_h = 10, \qquad b_h = 4.5, \qquad c_h = 3, \qquad B_h = \sqrt{5}. \tag{19}
$$

Equations 6–10 are iterated (up to a maximum of 50 times) until the following convergence conditions are met:

$$
\max\left[\|\frac{u_{*i} - u_{*i-1}}{u_{*i}}\|, \quad \|\frac{T_{*i} - T_{*i-1}}{T_{*i}}\|, \quad \|\frac{q_{*i} - q_{*i-1}}{q_{*i}}\|, \quad \|\frac{L_{*i} - L_{*i-1}}{L_{*i}}\|\right] < 0.001. \tag{20}
$$

The value of ${C_n}^2$ is then computed from standard stability-dependent similarity relations.

## 1.4 TurbZr

The TurbZr model was developed by ARL on the basis of the MARIAH MO scaling length $L$ formulation[3] and a report by Tofsted et al.[4] relating the MO scaling length to the optical turbulence parameter ${C_n}^2$. The development of the TurbZr model is very similar to that of the NAVSLaM model, except that TurbZr uses a single pass to compute $L$ rather than the iterated approach employed by NAVSLaM. The MARIAH approach begins with the expression for $L$ that includes the effect of atmospheric moisture:

$$L = \frac{{u_*}^2 \, \theta_v}{k \; g \, \theta_v^*}, \tag{21}$$

where, as previously, $k = 0.4$ is the von Karmann constant, $g$ is the local gravitational acceleration, $u_*$ is the friction velocity, $\theta_v = \theta(1 + 0.61q)$ is the virtual potential temperature, $\theta_v^* = \theta_*(1 + 0.61\theta q_*)$ is the virtual potential temperature scaling constant, $\theta_*$ is the potential temperature scaling constant, $q_*$ is the specific humidity scaling constant, and $q$ is the specific humidity. The partial differential relations for wind speed $V$, potential temperature $\theta$, and specific humidity $q$ gradients may be expressed as

$$\frac{\partial V}{\partial z} = \frac{u_*}{k \; z} \; \phi_m \tag{22}$$

$$\frac{\partial \theta}{\partial z} = \frac{\theta_*}{k \; z} \; \phi_H \tag{23}$$

$$\frac{\partial q}{\partial z} = \frac{q_*}{k \; z} \; \phi_H, \tag{24}$$

where $\phi_m$ and $\phi_H$ are the stability-dependent dimensionless wind shear and lapse rate functions that will be defined in Eqs. 29, 30, and 32. The essence of the MARIAH approach is to discretize these relations and rearrange them to solve for the stability-dependent parameters:

$$u_* = \frac{k \, \Delta V}{\phi_m \, \Delta ln \; z} \tag{25}$$

$$\theta_* = \frac{k\ \Delta\theta}{\phi_H\ \Delta ln\ z} \tag{26}$$

$$q_* = \frac{k\ \Delta q}{\phi_H\ \Delta ln\ z}, \tag{27}$$

where, for two measurement levels $z_1$ and $z_2$, $\Delta V = (V_2 - V_1)$, $\Delta\theta = (\theta_2 - \theta_1)$, $\Delta q = (q_2 - q_1)$, and $\Delta ln\ z = (ln\ z_2 - ln\ z_1)$. With these results, the expression for $L$ becomes

$$L = \frac{\phi_H\ (\Delta V)^2\ \theta_v}{{\phi_m}^2\ g\ \Delta lnz\ (\Delta\theta + 0.61\ \theta\ \Delta q)} \tag{28}$$

For unstable boundary layer conditions ($z < L$),

$$\phi_m = \left(1 - 15\frac{z}{L}\right)^{-1/4} \tag{29}$$

$$\phi_H = \left(1 - 15\frac{z}{L}\right)^{-1/2} \tag{30}$$

so that $\phi_H = {\phi_m}^2$ and

$$L = \frac{(\Delta V)^2\ \theta_v}{g\ \Delta lnz\ (\Delta\theta + 0.61\ \theta\ \Delta q)}\ . \tag{31}$$

In stable conditions $(L > 0)$ ,

$$\phi_m = \phi_H = 1 + 5\frac{z}{L} \tag{32}$$

so that Eq. 28 assumes the rearranged form

$$L\ \phi_m = \frac{(\Delta V)^2\ \theta_v}{g\ \Delta lnz\ (\Delta\theta + 0.61\ \theta\ \Delta q)}\ . \tag{33}$$

Substituting Eq. 32 into Eq. 33 and rearranging,

$$L = \frac{(\Delta V)^2\ \theta_v}{g\ \Delta lnz\ (\Delta\theta + 0.61\ \theta\ \Delta q)} - 5\ z\ . \tag{34}$$

Note that $\theta, \theta_v$, and $z$ in Eqs. 31 and 34 are all specified at a single atmospheric level. In the original MARIAH paper,[3] this level was specified to be $z = z^* = (z_2 - z_1)/ln(z_2/z_1)$. In the operational TurbZr implementation of MARIAH used in this study, it was found that eliminating the $-5z$ term in the expression for the stable-condition $L$ and using using $z = z_1$ elsewhere provided values of ${C_n}^2$ that were closer to those measured in scintillometer data and had less scatter for stable conditions, with negligible impact for unstable situations. The reason for this departure from the original MARIAH algorithm will be the subject of future studies. With this proviso, the form of $L$ used in TurbZr is, for both unstable and stable conditions,

$$L = \frac{(\Delta V)^2 \; \theta_{v1}}{g \; \Delta lnz \; (\Delta\theta + 0.61 \; \theta_1 \; \Delta q)} \tag{35}$$

where $\theta_1 = \theta(z_1)$, $\theta_{v1} = \theta_1(1 + 0.61q_1)$, and $q_1 = q(z_1)$. One observation to make here is that temperature lapse rates are frequently small under stable conditions. In that event, the expression for $L$ can cause extreme variability or divide by zero errors. To guard against such eventualities that would cause an abnormally large or small value of $L$, the TurbZr data point computation of optical turbulence is rejected if $|\Delta V| < \epsilon$ or $|\Delta\theta| < \epsilon$, where $\epsilon = 0.01$.

In Tofsted's[4] development, the value of $L$ given above yields a value of ${C_n}^2$ given by

$${C_n}^2 = \frac{u_\star^4 \; A^2 \; p^2}{k^2 \; g^2 L^2 \; T^2} \; z_1^{-2/3} \; 4.9 \; F(z_1), \tag{36}$$

where $A = 79 \times 10^{-6}$ K/mb, $p$ is the atmospheric pressure (mb), T is the absolute temperature at $z_1$ (K), and

$$F(z_1) = \left(1 - \frac{z_1}{L}\right)^{-2/3} \tag{37}$$

for unstable ($L < 0$) conditions or

$$F(z_1) = 1 + \left(\frac{z_1}{L}\right)^{2/3} \tag{38}$$

for stable ($L > 0$) conditions.

### 1.5 Cn2Ct2

A Java-language program, Cn2Ct2, was developed that calculates the optical turbulence strength parameter ${C_n}^2$ on the basis of sonic anemometer and barometer inputs at a small region (∼20 cm radius) in space. The algorithm is based on a paper by Aristidi et al.[6] The purpose of this code is to provide a cross-check value of ${C_n}^2$ for the two-level NAVSLaM and TurbZr models for land-based locations.

The present version of the Cn2Ct2 program is not intended to run in near real-time, but it can be adapted for such purposes at a later point. The current version of the program analyzes a 1-h archive file of sonic and barometric data. The incoming sonic data are sampled at 20 Hz, with the barometric data sampled over a longer time scale. As noted in Section 1.1, a more detailed exposition of this method, implementation, and results will be deferred to a subsequent report.

### 1.6 Uncertainty Estimates of Model Results

The uncertainty of TurbZr model estimates for ${C_n}^2$ has been derived from standard propagation of error analysis for the constitutive model equations developed in Rachele et al.[3] and Tofsted et al.[4] The resulting variance for $C_n^2$ is

$$\sigma^2_{C_n^2} = 16\left(\frac{C_n^2}{u_*}\right)^2\sigma^2_{u_*} + 4\left(\frac{C_n^2}{p}\right)^2\sigma^2_p + 4\left(\frac{C_n^2}{L_{ob}}\right)^2\sigma^2_{L_{ob}} + 4\left(\frac{C_n^2}{T}\right)^2\sigma^2_T + \left(\frac{C_n^2}{F}\right)^2\sigma^2_F \tag{39}$$

where

$$\sigma^2_F = \begin{cases} \frac{4}{9}\left[1-7(z/L_{ob})\right]^{-10/3}\cdot\left[49(z^2/L_{ob}^4)\right]\sigma^2_{L_{ob}} & L_{ob} < 0, \\ \frac{4}{9}\cdot 5.76(z^{4/3}/L_{ob}^{10/3})\sigma^2_{L_{ob}} & L_{ob} > 0. \end{cases} \tag{40}$$

$F$ is defined in Tofsted et al.[4] Equation 39 is expressed in terms of the input variables and the model-computed value of $C_n^2$.

A follow-up report will provide the full exposition of the analysis used to derive Eqs. 39 and 40.

## 2. Overview of Test Environment

### 2.1 Terrain and MSA Deployment

The field comparison test was conducted over multi-day time blocks during August to November 2021 (Phase 1) and July 2022 (Phase 2) near Las Cruces, New Mexico, at the United States Department of Agriculture (USDA) Jornada Experimental Range (JER, https://jornada.nmsu.edu/) installation of the ARL MSA.

The panoramic view of Fig. 1 shows that the JER terrain is dominated by mesquite clumps that are several meters in size and spacing. These mounds are approximately 1–2 m in height above the nearly bare sandy soil in between. On a larger scale, as shown in Fig. 2, the core MSA tower cluster used in this experiment is situated between the Dona Ana Mountains and Rio Grande Valley to the southwest and a much taller mountain range (the San Andres Mountains) to the east.

**Fig. 1 Panoramic view of typical JER terrain (from the JER web site, https://jornada.nmsu.edu/)**

### 2.2 General Weather Conditions for Test Periods

The fall (Phase 1) and summer (Phase 2) periods of the NATurE test presented two disparate seasonal weather profiles. In the JER region, fall conditions are typically drier, less cloudy, and less windy than other times of year. The timing of the summer portion of the test (early July 2022) coincided with the advent of monsoonal weather, with mostly cloudy conditions during afternoon hours and occasional thundershower activity. Thunderstorm cells forming in the monsoonal period usually produce localized downdraft wind fields and highly variable wind vectors.

The actual weather that occurred during the two phases of the experiment was atypical in some ways. Winds were generally light to moderate during Phase 1, but the last half of this period was partly to mostly cloudy, in contrast to fall norms. Phase

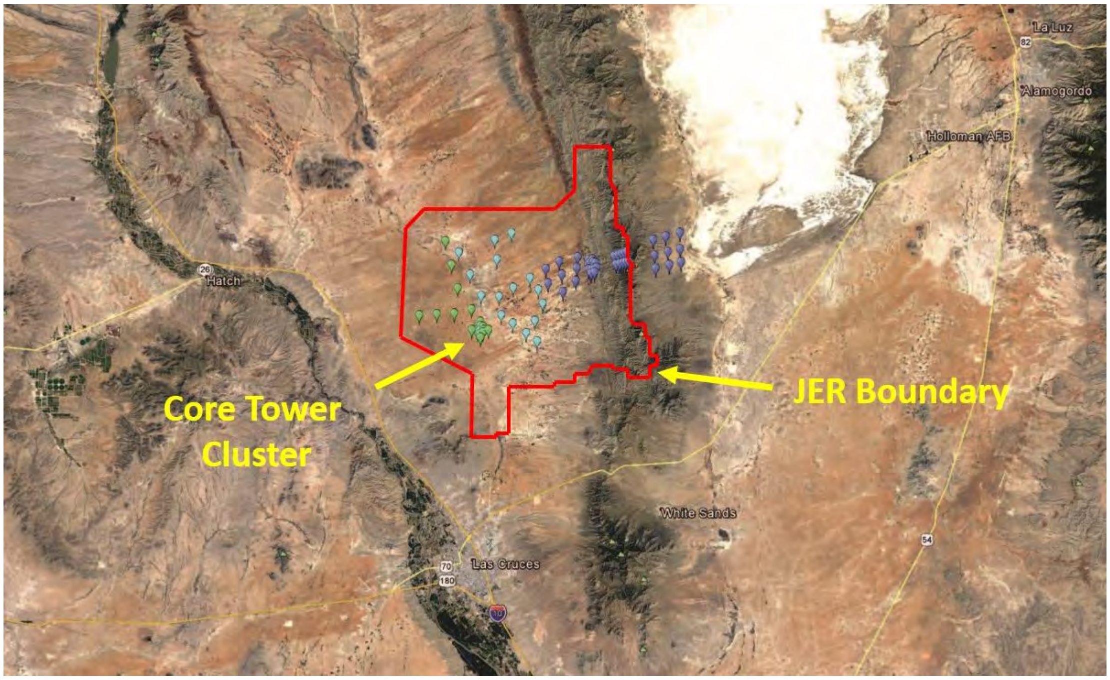


**Fig. 2 Planned layout of MSA towers for MSA deployment Phases 2 (green) and 3 (blue and purple) at the JER (approximate outline in red)**

2 was also partly to mostly cloudy in the afternoon, but thunderstorm activity was reduced from the daytime normal and winds were lighter than customary for several days in the observing period.

## 3. Test Equipment and Plan

### 3.1 Equipment

Sensors that were used in this experiment consisted of previously deployed 10-m MSA tower sensors in the MSA core (Towers 1–12) and additional sensors specifically for NATurE. Unfortunately, sensors on the 30-m central MSA core tower (Tower 36) were not available for either phase of NATurE. Consequently, a 10-m temporary tower (Tower 36A) was deployed next to Tower 36 for comparisons with the SLS 40A scintillometer (also set up next to Tower 36).

### 3.2 MSA Tower Sensors

The standard MSA tower is equipped with sonic anemometer sensors (Gill 3D WindMaster) situated at 2 and 10 m AGL. These provide measurements of (u, v, w) wind components, speed of sound, and ambient air temperature at a data output rate of 20 Hz. Thermistor and humidity probes are also mounted at 2 and 10 m AGL, providing air temperature and humidity measurements at a data output rate of 1 Hz. At the base of the tower is an enclosure that contains an atmospheric pressure sensor and a Campbell Scientific data logger for the 1-Hz temperature, humidity, and pressure data streams. Each tower is also equipped with a radio transmitter that sends data to local servers that archive the sensed meteorological data. Tower 36A lacked the radio connection to the MSA data network, but otherwise had a similar suite of sensor devices. Data in this instance were logged at the tower and collected in batches via periodic hardwire connection. The time zone at which the data were time-stamped was Mountain Standard Time (MST). Both phases of NATurE were conducted when Daylight Savings Time (DST) was in effect, so MSA sonic anemometer and logger data were carefully adjusted to MST. Tower 36A data were also adjusted to an MST date/time standard. Figure 3 shows Tower 36A as it was configured for Phase 1 of NATurE.

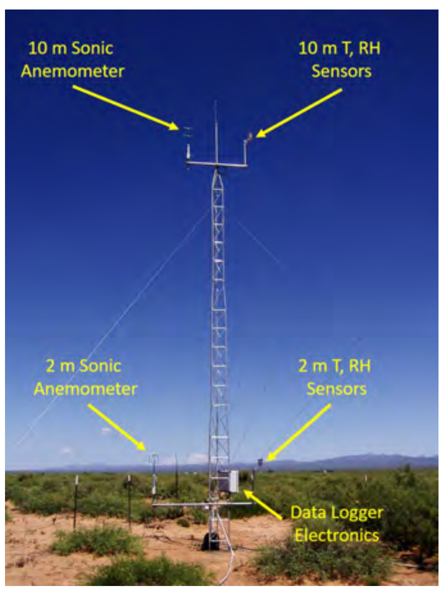


**Fig. 3 NATurE temporary 10-m tower ("Tower 36A") next to MSA 30-m Tower 36 at the JER**

## 3.3 BLS 450 Scintillometer

A Scintec Model BLS 450 scintillometer was set up in an east–west orientation for Phase 1. This model differs from the BLS 900 in its single aperture transmitter configuration, which does not measure crosswind data. Figure 4 shows the Phase 1 setup with the transmitter at MSA Tower 1 and the receiver at Tower 2. The orientation of this device was changed to a north–south direction for Phase 2. The scintillometer baseline was approximately 2 km for both phases of NATurE. The BLS baseline was elevated approximately 4 m above the surrounding terrain and thus had to be scaled via a power law correction to the NAVSLaM/TurbZr reference height of 2 m AGL. Operationally, a power law correction with an exponent of –4/3 was used for the entire diurnal cycle. A –2/3 power law correction was attempted for the nighttime data, but it made little difference due to the large turbulence fluctuations that were observed at night.

**Fig. 4 Phase 1 BLS 450 setup at MSA towers; BLS transmitter at Tower 1 (left) and BLS receiver at Tower 2 (right)**

## 3.4 SLS 40A Scintillometer

A short path Scintec Model SLS 40A scintillometer was set up next to Tower 36A, oriented parallel to the BLS baseline. This instrument was only available for Phase 1 due to damage to its transmitter/receiver data cable at the end of Phase 1. Figure 5 shows the transmitter/receiver line of sight, which was approximately 125 m long. This device provided an estimate of the inner scale of turbulence as well as ${C_n}^2$. The proximity of the SLS baseline to the tops of mesquite mounds along the path was a factor of some concern. Perhaps for this reason, the resulting ${C_n}^2$ measurement from this device did not compare well with the model results during stable nighttime conditions. The nominal elevation of the SLS baseline was about 1.7 m, so that any power law correction to the 2-m model reference height had minimal effect.


**Fig. 5 Phase 1 SLS 40A setup at MSA Tower 36; view from SLS transmitter (left) and view from SLS receiver (right)**

### 3.5 Pyranometers

Kipp and Zonen pyranometers at MSA Towers 22 and 27 were not formally part of this experiment, but their daily measurements of solar irradiance are displayed here for the Phase 1 of NATurE. These data are useful in assessing the degree of cloud cover that prevailed at given times of day over the MSA.

### 3.6 Tower 1 Camera

A horizontally oriented, westward-pointing camera was located on MSA Tower 1. This camera thus pointed in the direction of the scintillometer baselines for Phase 1. As no all-sky camera was available for Phase 1, this sensor was used to assess the type of cloud cover that occurred during the dates covered by this phase. Hourly images for this Phase 1 sensor are presented in the Appendix.

### 3.7 Tower 36A All-Sky Camera

An all-sky "fisheye" imager was available and used for Phase 2 of the experiment near Tower 36A. This sensor was much better at depicting overall cloud conditions during the day, but nighttime cloud cover could not be discerned due to the sensitivity limits of the camera. Daytime results for this device on 6 July 22 are shown in the Appendix.

## 4. Layout of NATurE Experiment

The 13-tower central cluster of the MSA (Fig. 6) was selected for this field study due to its higher sampling density, relatively uniform terrain properties, and ease of access. All towers used for this study had sonic anemometer and thermistor sensors at 2- and 10-m AGL heights, although a few of the towers (Towers 1, 2, 4, and 8) had sensor data issues and were not included. Figure 7 displays the relative location of the two pyranometer sites (Towers 22 and 27), 5.1 km northeast and 5.5 km west of Tower 36A, respectively.

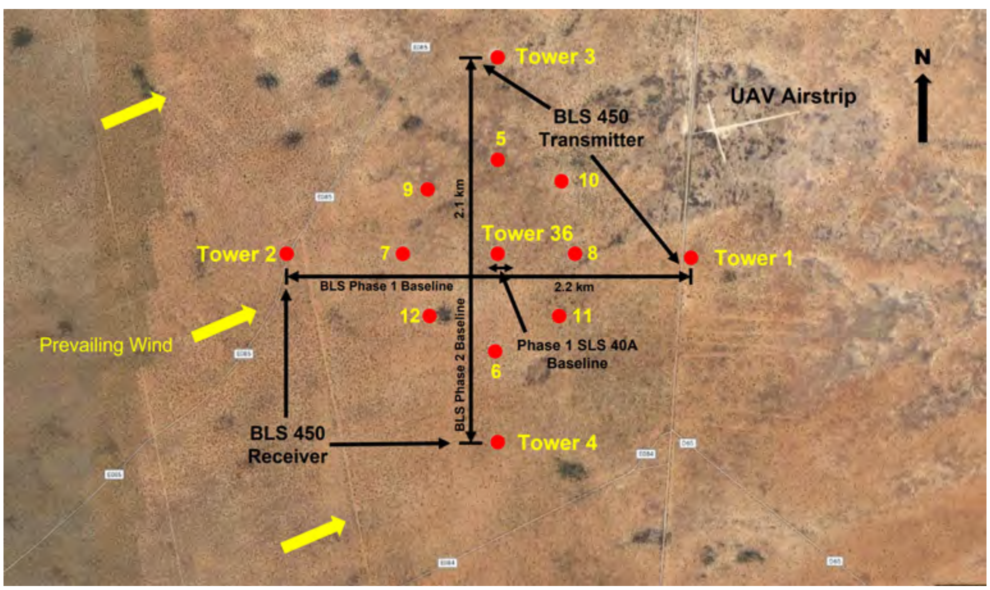


**Fig. 6 Layout of MSA core tower cluster and NATurE Phases 1 and 2 BLS/SLS scintillometer baselines at the JER**

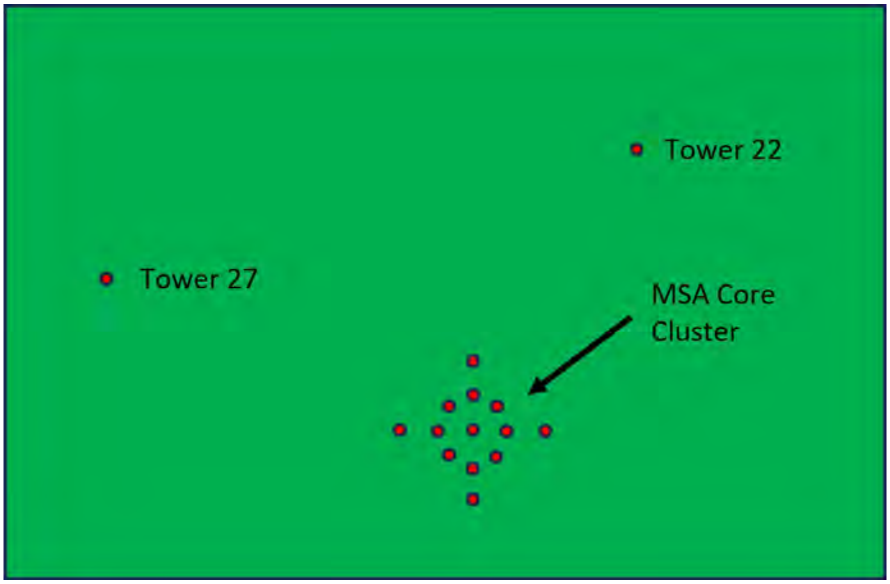


**Fig. 7 MSA pyranometer tower locations relative to central cluster**

## 4.1 Phase 1

Prevailing winds in the region during fall, winter, and spring are typically from the southwest. The Phase 1 scintillometer configuration was arranged on an east–west orientation to allow for prevailing winds to be nearly parallel to the scintillometer baselines. The motivation for this setup is that additional analysis may reveal propagation of large turbulent structures as time correlations across the array.

## 4.2 Phase 2

The north–south orientation of the Phase 2 scintillometer baselines was designed to examine the possibility of large-scale drainage flows from nearby north–south mountain ranges or downdrafts from thunderstorm cells that build up over these ranges.

## 5. Experiment Schedule

### 5.1 Phase 1

As mentioned previously, Phase 1 data collection days at the end of October and the beginning of November 2021. Specifically, 28–31 October and 1–2 November constituted a 6-day data collection period, with 27 October was used as a setup day and 3 November as a shutdown day. Problems with setting up the SLS 40A scintillometer persisted into the morning of 28 October, so only afternoon data were available for that day. On 3 November, rodent damage to the SLS transmitter/receiver data line abruptly ended afternoon data. The SLS unit was then shipped to the manufacturer for repairs and was not available for the Phase 2 part of the test.

### 5.2 Phase 2

With the realignment of the BLS/SLS baselines to a north–south orientation for Phase 2 of NATurE, measurements were conducted in early July 2022. Data were collected on 6, 7, and 8 July for a 3-day measurement set. Of these, only the 6 July results are included in this report, with follow-up analysis reserved for a subsequent report.

## 6. Data Archives

MSA core cluster tower data for each MST day were archived by a central server in the JSON (JavaScript Object Notation) format, a standard text-based representation of structured data based on JavaScript object syntax. An MSA-specific JSON sample is shown in Fig. 8, where stream index 10, its time stamp, and data content are highlighted. The JSON key to the stream index identifies the associated MSA tower number, the sensor description, and the data format/meaning. In the case shown here (Fig. 9), the Tower 1 2-m AGL sonic u, v, w, speed of sound, and sensed air temperature data are given for a specific date/time. A Java-language parser was implemented that breaks a daily JSON data file into individual tower flat files for 2- and 10-m sonic sensors and slower logger-connected sensors. Obviously, when multiple towers and sensors operating at up to 20 Hz are involved, a daily text file can become quite large and parsing times are measured in minutes on a typical PC. Consequently, a more portable, more efficient, and more versatile Java version of the JSON parser was written by one of the coauthors (Johnson) for future use in MSA-related experiments.

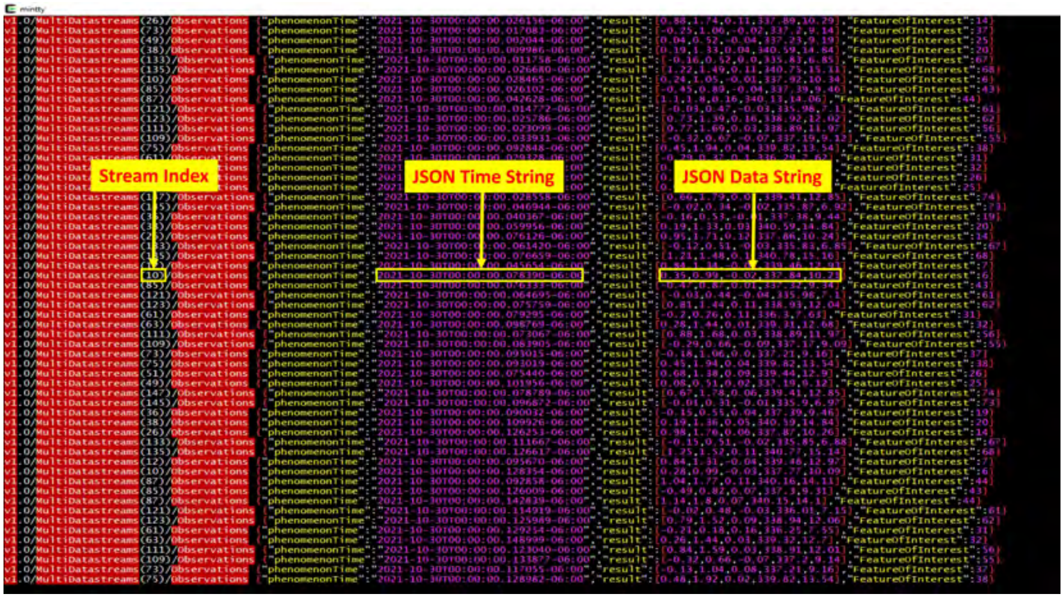


**Fig. 8  Example of MSA JSON-format data with critical fields highlighted**

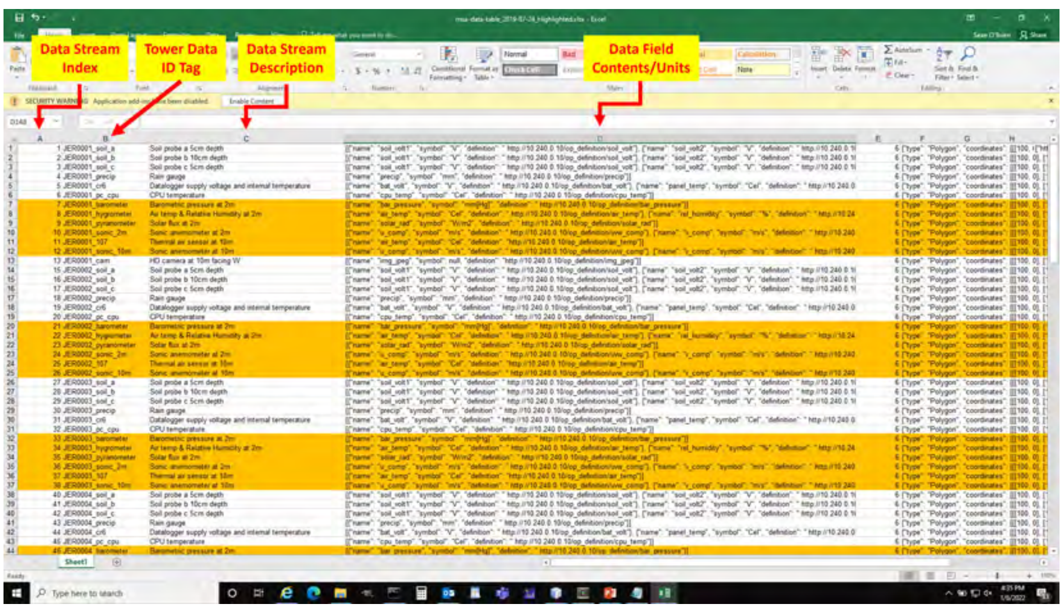


**Fig. 9  Example of field key for MSA JSON format**

## 7. Reduction and Analysis Approach

Before comparing any of the model results with scintillometer data, the data set was reviewed to discover any anomalies that might affect the validity of comparison results. This process also eliminated MSA tower data that had significant time gaps, had values out of credible ranges, or were entirely absent. Next, the models were adapted to accept input data from the valid MSA core towers and Tower 36A. Reduction software was implemented that combined 1-Hz logger data for temperature, relative humidity, and atmospheric pressure with 20-Hz sonic anemometer (u, v, w) and temperature data into averaged 1-min sampling interval data sets that NAVSLaM and TurbZr could use. The BLS and SLS scintillometer data were also cast into a format that was directly importable to Excel spreadsheets for comparison with model results.

## 7.1 Data Review

Two of the fundamental quantities that drive the NAVSLaM and TurbZr models are the near-surface temperature and wind speed gradients. The wind speed gradient between 2 and 10 m AGL is provided by short time interval (1-min) averages of sonic anemometer wind speed, averaged at each level prior to computing the gradient delta. For the temperature gradient averages over 1 min, two choices are available: fast (20 Hz) sonic anemometer temperature and temperature measured by the slower (1 Hz) thermistor sensors that are recorded on a data logger attached to each tower. Before implementation of the data reduction routines that provide temperature gradient inputs to the models, it is a good idea to compare the sonic/thermistor 2-/10-m temperature gradient data to see which is more consistent and accurate across the tower array in the central MSA cluster. It is surprising that major inconsistencies arise in such a comparison, as evidenced by Figs. 10 and 11.

Figure 10 displays examples from the 31 Oct 2021 data set where major disparities between the sonic and thermistor ("logger") data are apparent for Towers 3, 5, 11, and 36A. The thermistor data do, however, show reasonable tower-to-tower consistency during the daylight hours for this tower set. The two data sources do show good to excellent equivalence on the same date for Towers 7, 9, and 10 (Figure 11). On the basis of these results, it was decided that the thermistor ("logger") data would be used to compute temperature gradients for Towers 3, 5–7, and 9–12. Towers 1, 2, 4, and 8 were excluded from the reduction and analysis due to data dropouts or obviously erroneous sensor outputs. Strangely, Tower 36A daytime sonic temperature gradients agreed better with the thermistor measurements for the other towers; in that case, the *sonic anemometer* data were used to compute temperature gradients for the models.

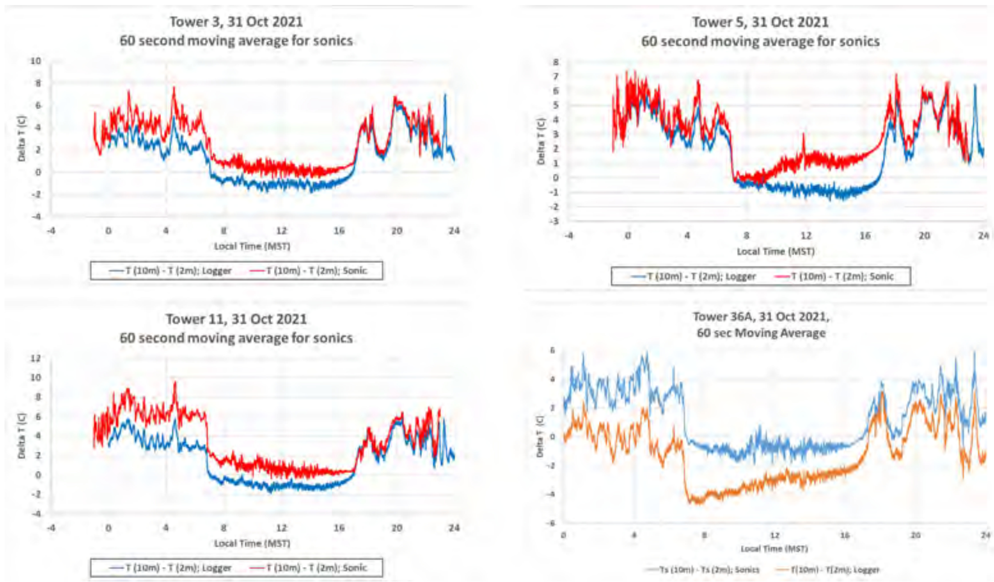


**Fig. 10 Examples of poor agreement between sonic anemometer and thermistor probe temperature gradients, 31 Oct 2021**

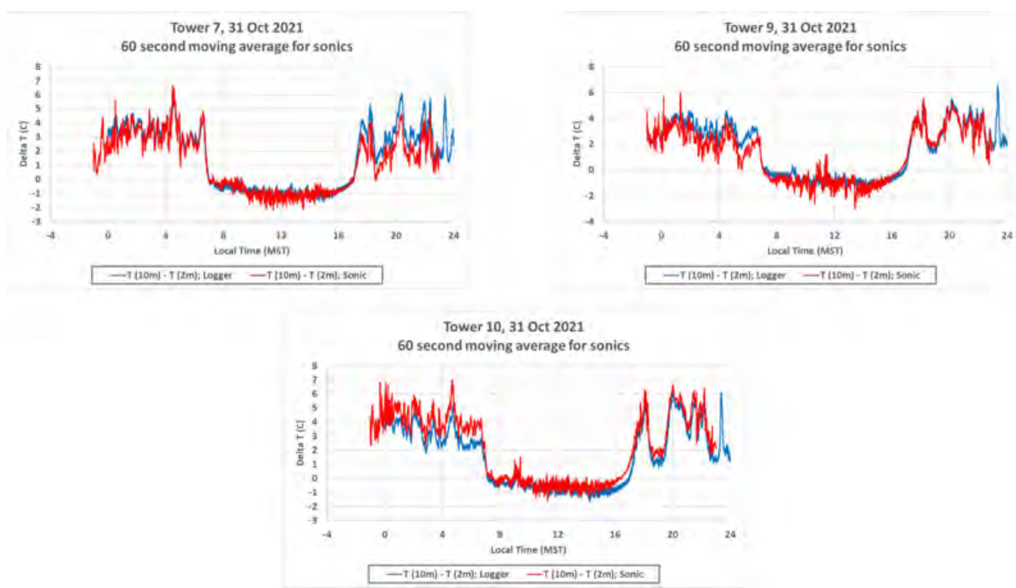


**Fig. 11 Examples of good agreement between sonic anemometer and thermistor probe temperature gradients, 31 Oct 2021**

## 7.2 NAVSLaM Setup and Output

At an early point in setting up the software for this study, it was decided that modifications to the NAVSLaM MATLAB code should be minimal, with no translation of the original MATLAB code or creation of a runtime interface to another computer language. Only a small MATLAB driver routine was written to read data from an input file (MSAData.txt) generated by TurbZr, with nearly identical content to that used as input by TurbZr. These input data consisted of 1-min average wind speed, air temperature, and absolute humidity at 2 and 10 m AGL, as reduced from MSA tower 1-s (logger temperature, relative humidity, and air pressure 2 and 10 m AGL) data and 20-Hz (sonic anemometer temperature and u,v,w wind component 2 and 10 m) data.

The customized NAVSLaM driver invoked the two-level version NAVSLaM_20-_2lev_180816 of the NAVSLaM model using a data table generated from the input file. Optical turbulence $C_n^2$ NAVSLaM results at each 1-min time interval were output to a text file, Cn2.txt, which could be directly incorporated into an analysis spreadsheet.

### 7.3 TurbZr Setup and Output

A parser (JSONTest.java) was written to process the large daily JSON MSA data archive files (that contain both 20-Hz sonic and 1-Hz logger data at 2- and 10-m levels) into individual tower output flat text files with formats compatible for input to TurbZr and for environmental parameter plots. The files used for input to TurbZr were averaged over 1-min. The environmental parameter output files were formatted at their native sampling rate (i.e., 20 Hz for the u, v, w, wind components and ambient temperature T sonic data in separate 2- and 10-m AGL tower files) and 1-Hz logger data for temperature, relative humidity, and atmospheric pressure. These native sampling rate files could be easily imported into spreadsheets and averaged over arbitrary averaging windows. The 1-min sampling interval files for individual towers were then used as input for TurbZr. The output from TurbZr was in the form of hour-of-day and corresponding $C_n^2$ value, in a format easily importable to spreadsheets for plotting and analysis. TurbZr also exported a file for subsequent input to NAVSLaM, as noted previously.

### 7.4 Scintillometers

Where necessary, scintillometer data were concatenated from hourly individual files into daily files suitable for export to spreadsheets.

### 7.5 Sonic Anemometers

Wind speed and direction data were generated at the 1-min intervals by a program named WindDirectionByMinute.java. The 20-Hz u, v, w wind components were averaged to a 1-min window before computing speed and direction values for each minute. The daily wind speed and direction outputs were then saved in individual tower files readily incorporated into spreadsheet formats.

## 8. Results

### 8.1 Illumination and Sky Conditions

Table 1 lists the sunrise, sunset, morning and evening neutral event (NE) times for the JER unmanned aerial vehicle (UAV) airstrip that lies just to the east of the MSA core cluster. The approximate morning and evening NE times are computed as 40 min after sunrise and 80 min before sundown, as is customary for this region under clear conditions.

**Table 1 Sunrise, sunset, and nominal neutral event times for JER UAV airstrip; Phase 1 and 2 dates**

| Date | Sunrise (MST) | Sunset (MST) | Morning NE (MST) | Evening NE (MST) |
|---|---|---|---|---|
| 28 Oct 2021 | 0621 | 1720 | 0741 | 1640 |
| 29 Oct 2021 | 0622 | 1719 | 0742 | 1639 |
| 30 Oct 2021 | 0623 | 1718 | 0743 | 1638 |
| 31 Oct 2021 | 0624 | 1717 | 0744 | 1637 |
| 01 Nov 2021 | 0625 | 1716 | 0745 | 1636 |
| 02 Nov 2021 | 0626 | 1715 | 0746 | 1635 |
| 06 Jul 2022 | 0505 | 1918 | 0625 | 1938 |

The first 3 days of the Phase 1 (28–30 Oct 21) period were essentially clear, as indicated by the Towers 22/27 pyranometer measurements of solar irradiance in Fig. 12. There were a few upward and downward excursions due to instrumental anomalies, but these were few and insignificant. The last 3 days of Phase 1 featured partly cloudy skies, as apparent in Fig. 13. Figure 14 contrasts the irradiance for clear days (30 Oct for Tower 22 and 29 Oct for Tower 27) with that for a cloudy day (1 Nov). The top row of plots shows the entire day irradiances (red for the clear day, blue for the cloudy day, and amber for the residual irradiance: cloudy minus clear). The bottom row shows these same quantities on an expanded time scale, from 1300 to 1500 MST.

There are significant positive excursions (up to 200 W/$m^2$)in the residuals, indicating strong contributions from scattered (diffuse) irradiance to the direct beam irradiance. Lateral scattering from the sides of thicker clouds and forward scattering from thinner clouds are the likely contributors to the positive residuals. The 1300–1500 MST plots indicate a noticeable positive residual near 1315 and a negative excursion near 1345 for both Towers 22 and 27. The westward-pointing camera on Tower 1 depicts the visual appearance of the terrain at 1315 and 1345 (Fig. 15). The 1315 image shows direct beam shadowed terrain features while the 1345 image does not. Given the significant separation between Tower 1 and Towers 22/27, this might indicate a widespread cloud field feature that crossed over the MSA. Of course, this is conjectural in the absence of detailed all-sky camera and solar aureole radiance measurements. The effect on optical turbulence for these residual fluctuations is not immediately apparent and probably has some degree of latency in the surface energy budget response. Both the BLS and SLS measurements do show noticeable local minima near 1300 and shortly after 1400 (see the 1 November plots, Figs. 24 and 25), but just how or if these correlate with a positive irradiance residual excursion is not known and probably cannot be determined unless the scintillometer baselines are in closer proximity than was the case for the NATurE experiment.

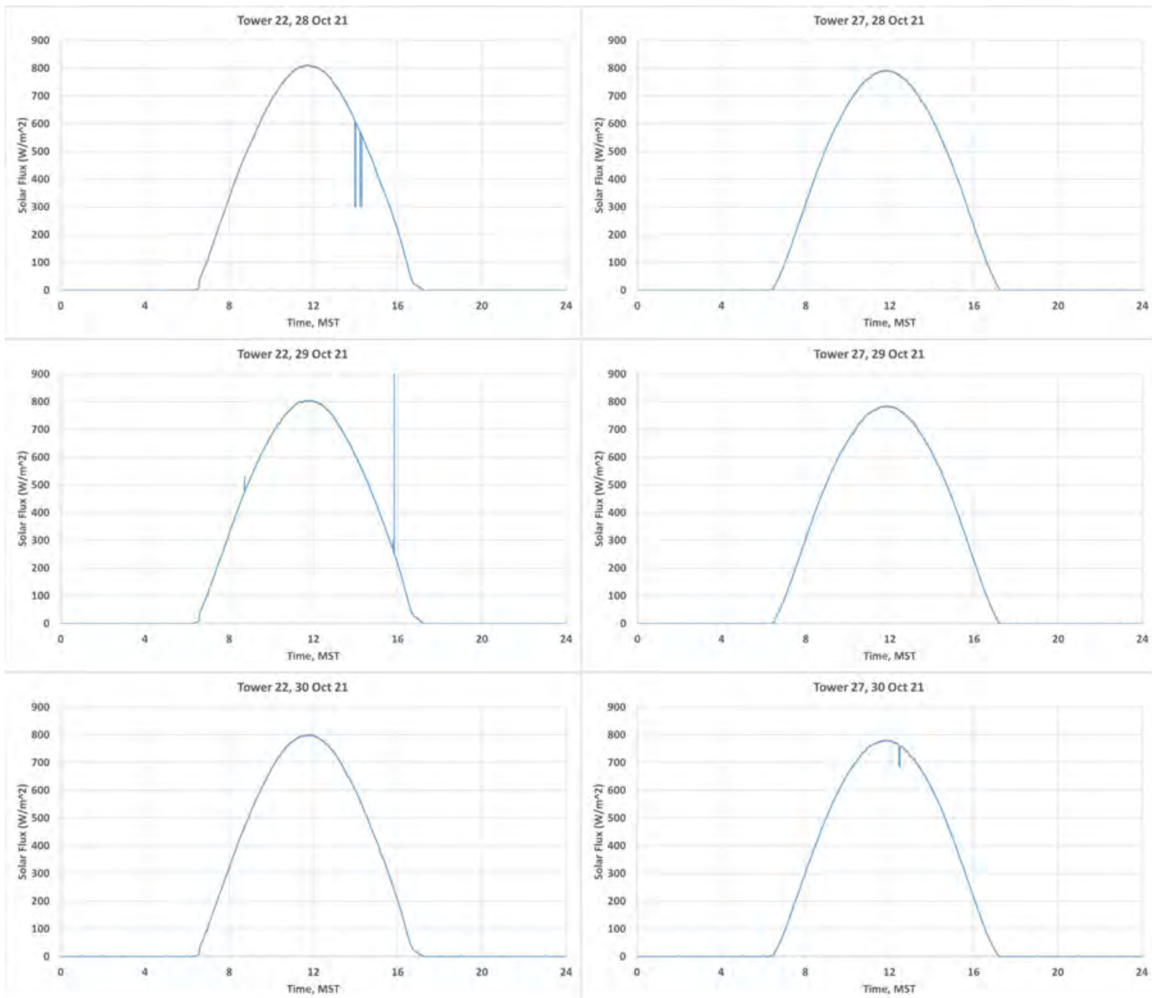


**Fig. 12 NATurE Phase 1 clear day irradiances**

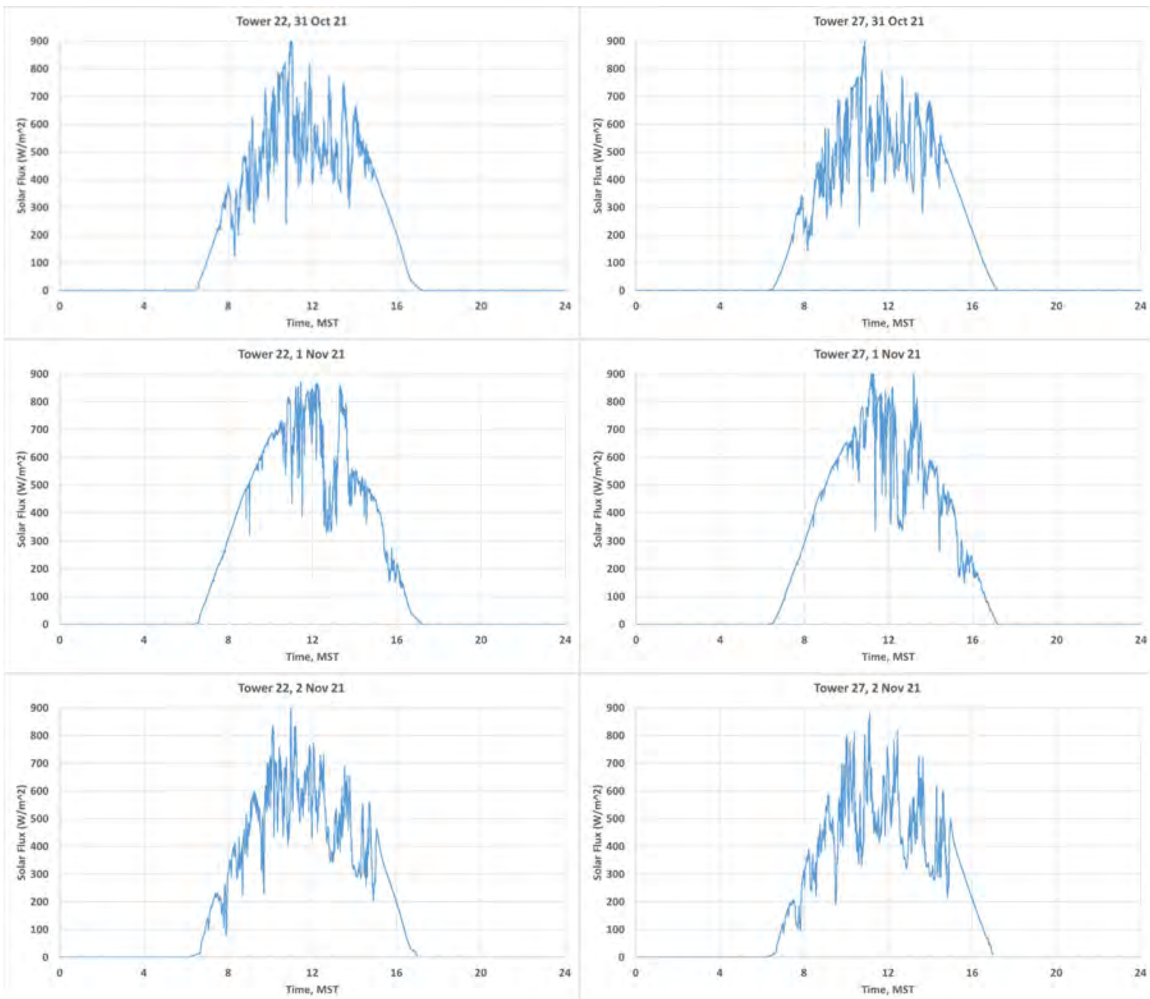


**Fig. 13 NATurE Phase 1 partly cloudy day irradiances**

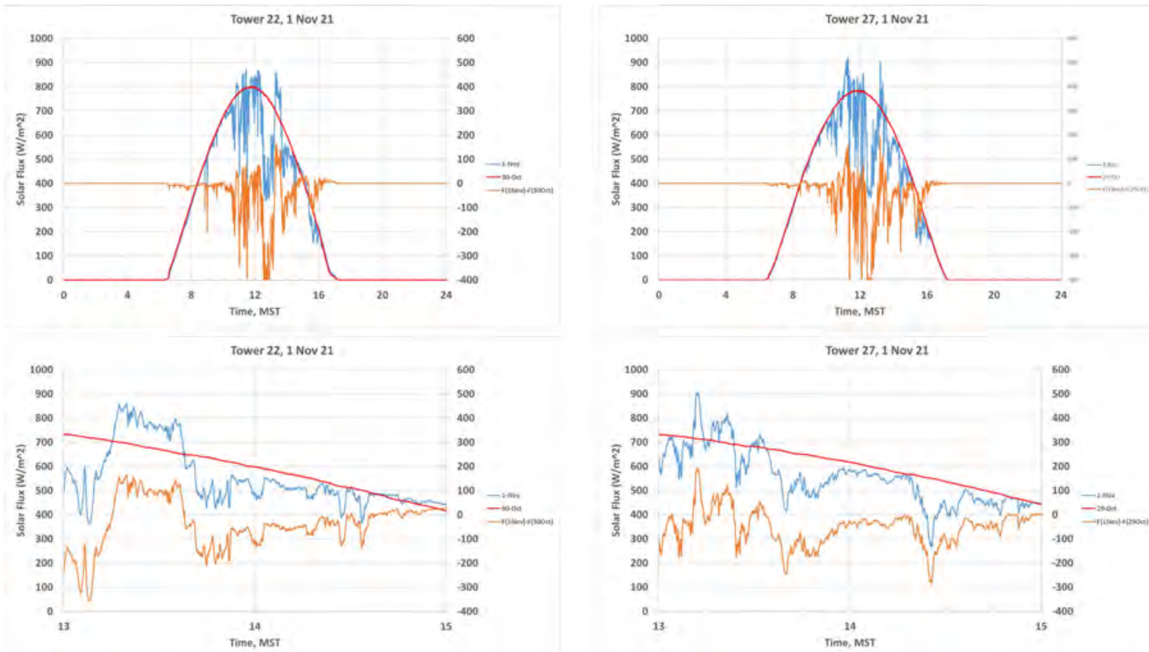


**Fig. 14 Comparison of clear and partly cloudy day irradiances, 1 Nov 21**


1315: Direct + Diffuse

1345: Diffuse

**Fig. 15 Comparison of Tower 1 clear and partly cloudy terrain images, 1 Nov 21**

## 8.2 BLS/SLS Scintillometer Measurements

### 8.2.1 Basic Data, Phases 1 and 2

Diurnal Phase 1 measurements for the BLS and SLS scintillometers are shown in Figs. 16–27. In most cases, the evening NE minimum is more pronounced than the morning event, particularly for the SLS. For even time-averaged BLS data, nighttime values of ${C_n}^2$ show extreme variability (1–2 orders of magnitude) over periods of minutes, in contrast to daytime fluctuations, which are relatively smooth. Figure 28 depicts a diurnal BLS measurement for a Phase 2 example (6 July 22).

One item of concern is the accuracy and consistency of the BLS and SLS data when scaled to the same (2 m AGL) reference height. A spot check is shown in Fig. 29 for 30 Oct 21. In this instance, the scaled BLS data falls well below the SLS data, particularly during the daytime hours between NEs. There are multiple possibilities that might explain this lack of agreement. One cause might be a simple faulty calibration or configuration of either the BLS or SLS. Another cause might be that the –4/3 power law adjustment for height is incorrect and that the BLS was operating under stronger lapse conditions than specified. A third possibility could be that the SLS baseline path passed too close to the tops of mesquite clumps and sensed much higher optical turbulence than would be experienced over flatter terrain. Any explanation is clearly debatable, but a reasonable guess would be that a combination of the second and third factors were responsible for the observed anomaly. A more comprehensive comparison set needs to be constructed to see if this disparity is consistent over the entire experimental data set.

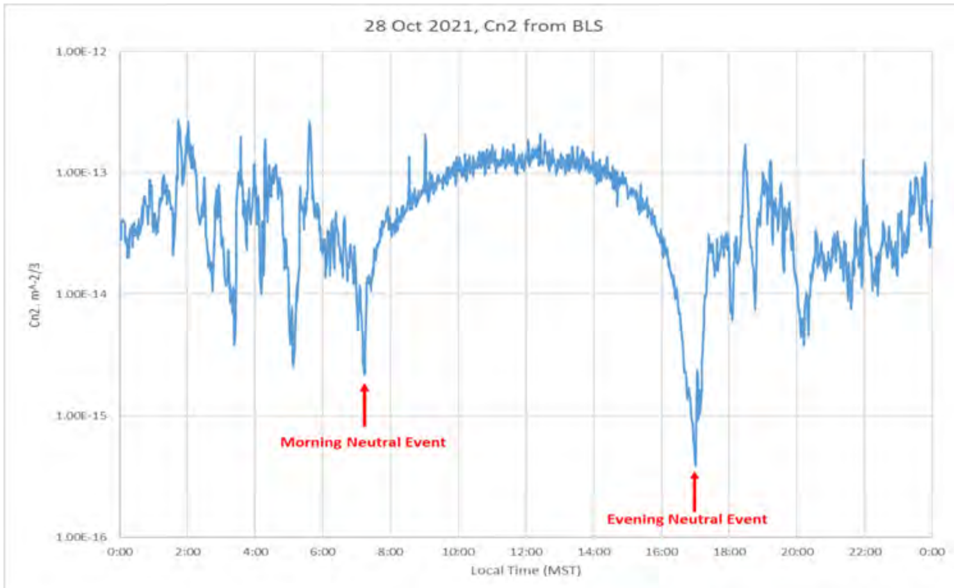


**Fig. 16  NATurE Phase 1 BLS measurements, 28 Oct 21**

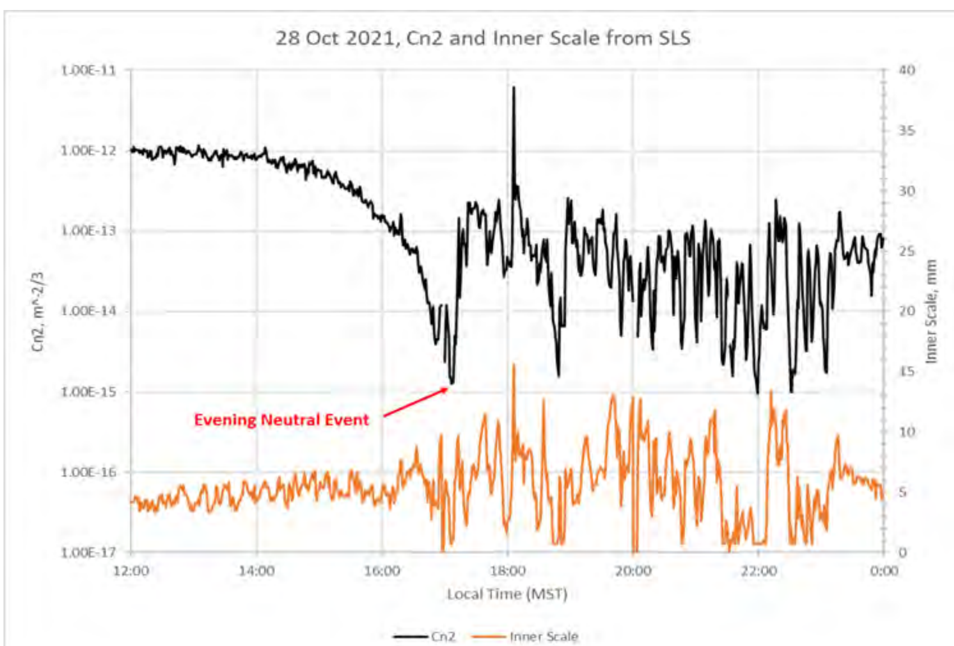


**Fig. 17  NATurE Phase 1 SLS Cn2 and inner scale measurements, 28 Oct 21**

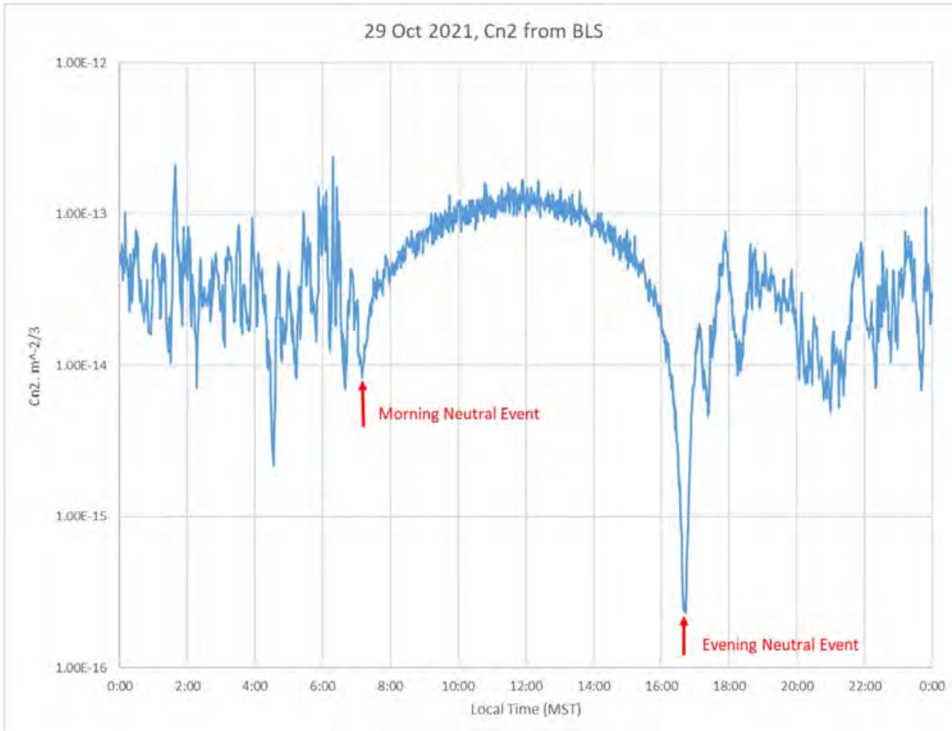


**Fig. 18 NATurE Phase 1 BLS measurements, 29 Oct 21**

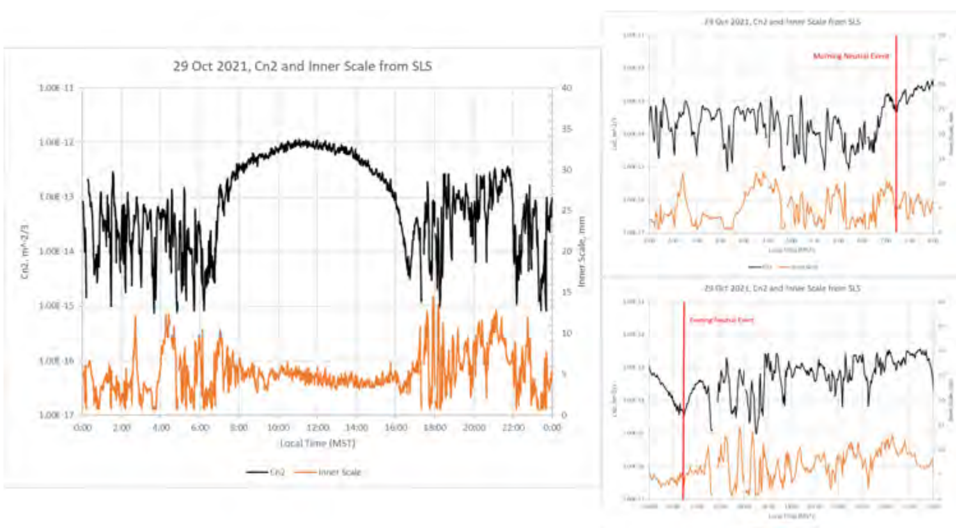


**Fig. 19 NATurE Phase 1 SLS Cn2 and inner scale measurements, 29 Oct 21**

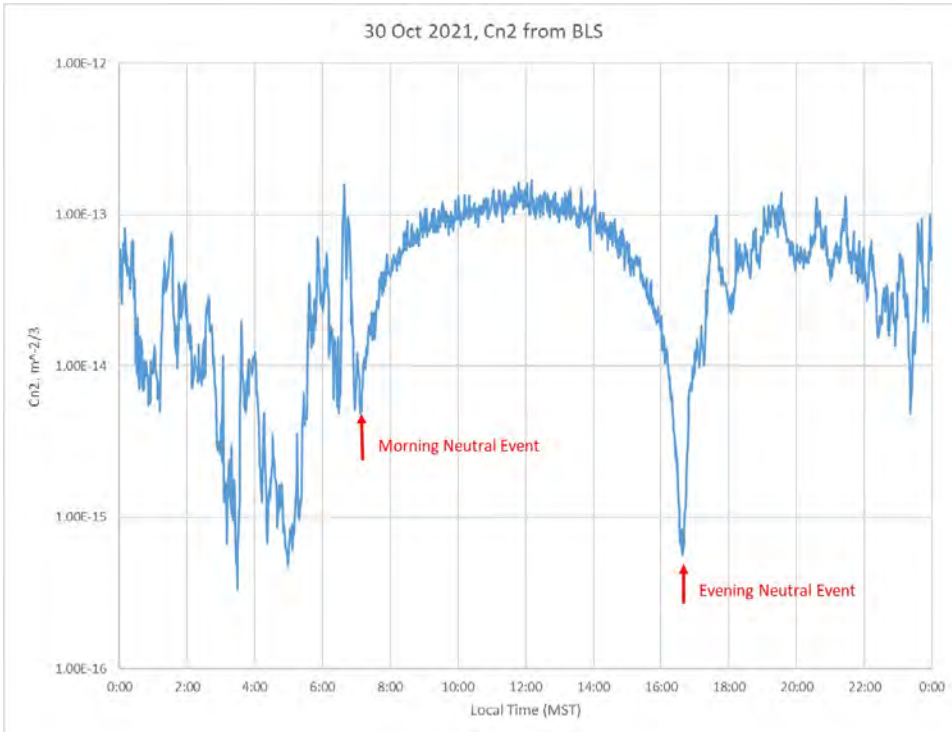


**Fig. 20  NATurE Phase 1 BLS measurements, 30 Oct 21**

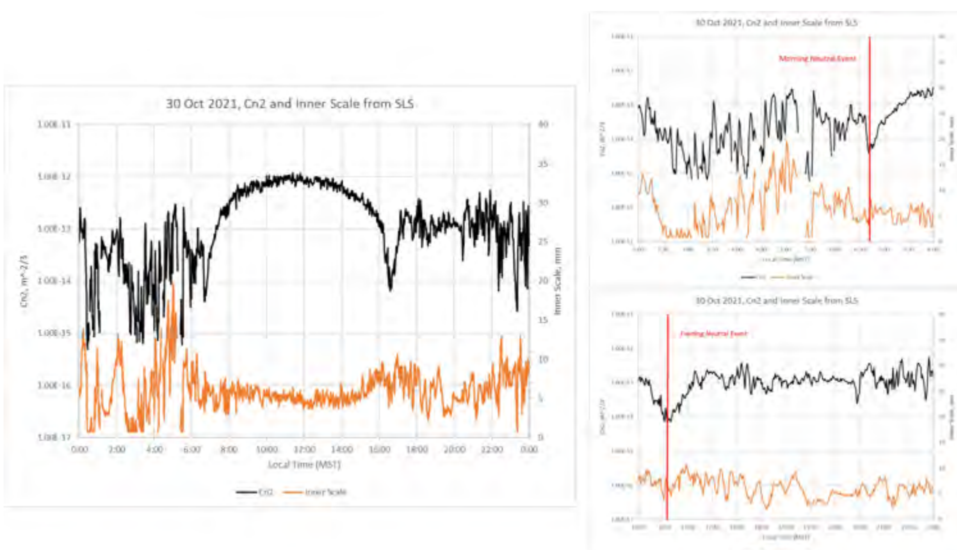


**Fig. 21  NATurE Phase 1 SLS Cn2 and inner scale measurements, 30 Oct 21**

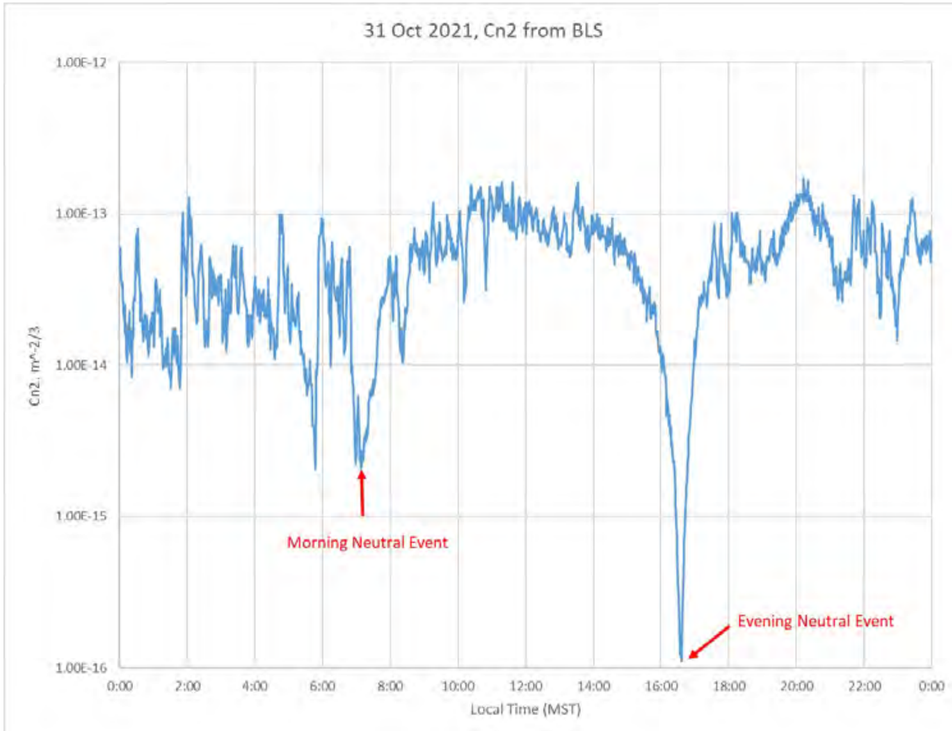


**Fig. 22 NATurE Phase 1 BLS measurements, 31 Oct 21**

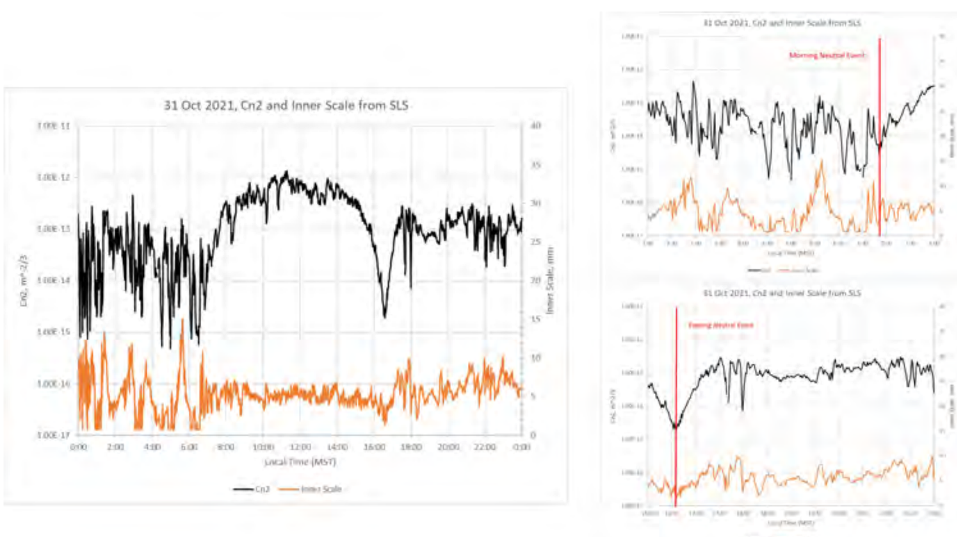


**Fig. 23 NATurE Phase 1 SLS Cn2 and inner scale measurements, 31 Oct 21**

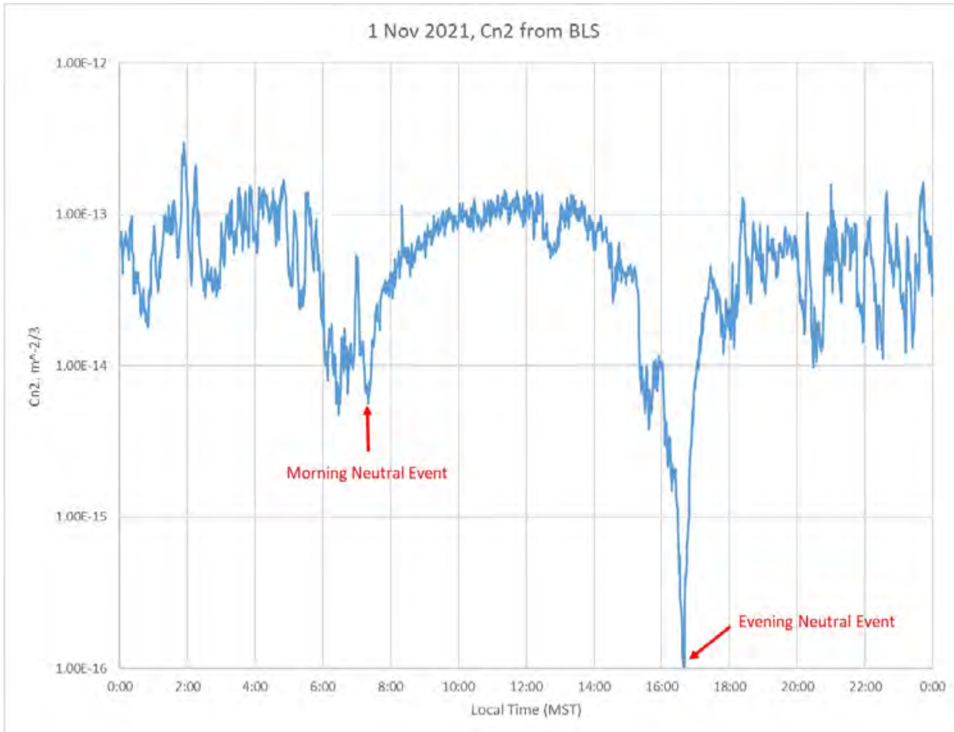


**Fig. 24  NATurE Phase 1 BLS measurements, 1 Nov 21**

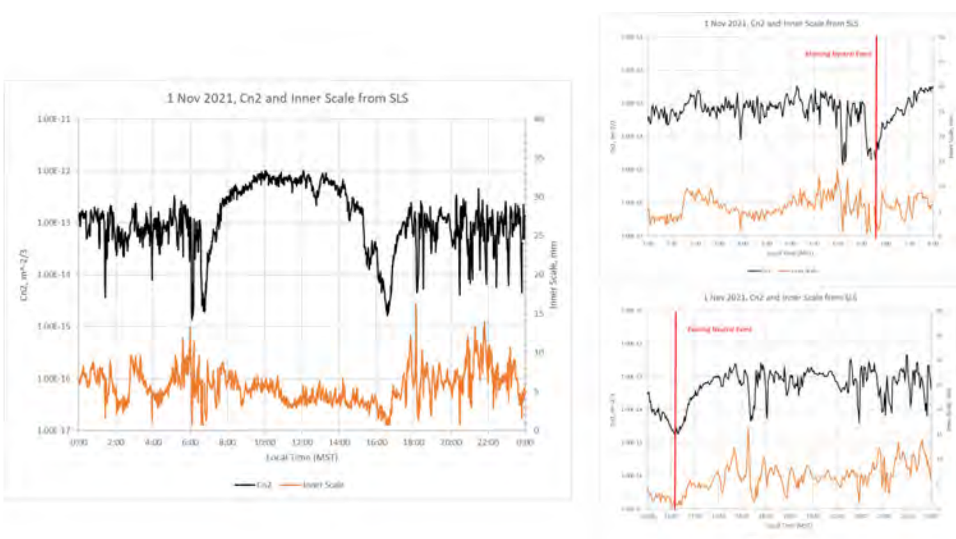


**Fig. 25  NATurE Phase 1 SLS Cn2 and inner scale measurements, 1 Nov 21**

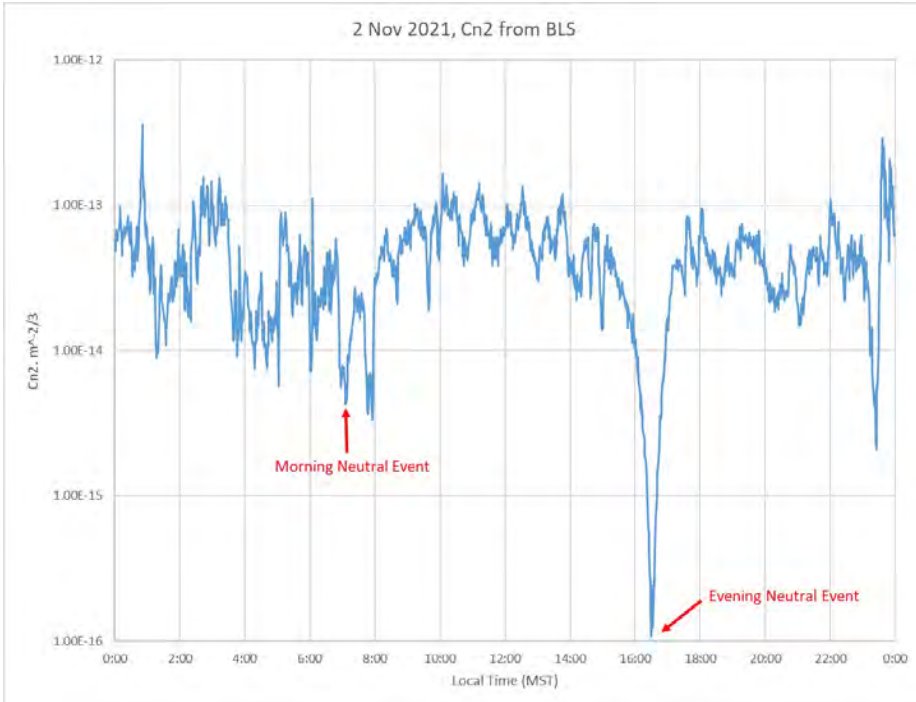


**Fig. 26  NATurE Phase 1 BLS measurements, 2 Nov 21**

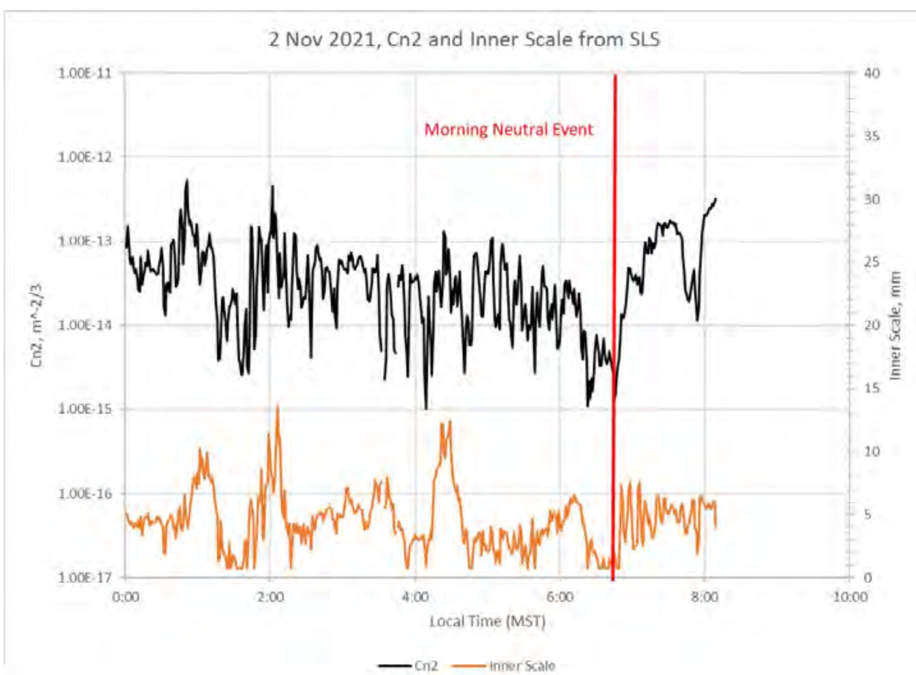


**Fig. 27  NATurE Phase 1 SLS Cn2 and inner scale measurements, 2 Nov 21**

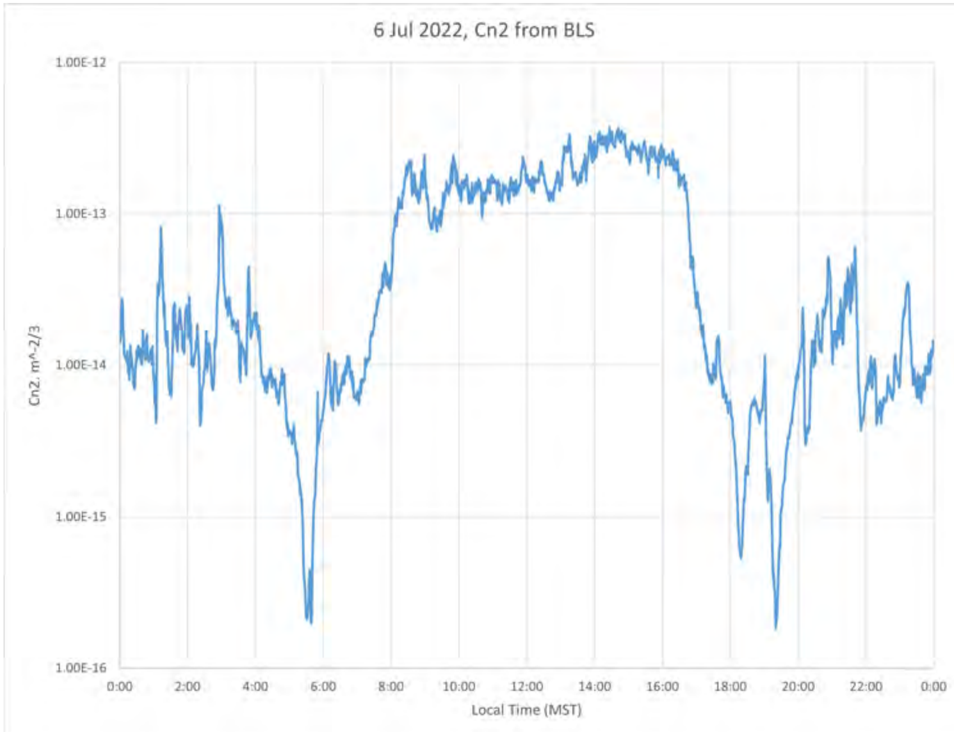


**Fig. 28 NATurE Phase 2 BLS measurements, 6 Jul 22**

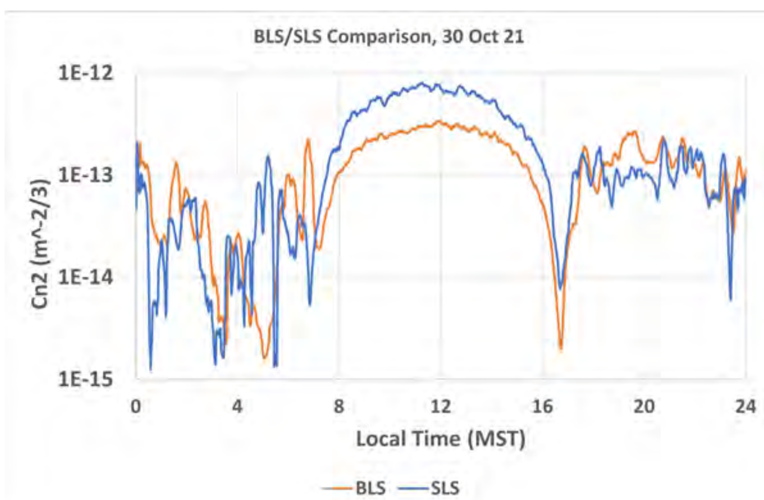


**Fig. 29 Comparison of BLS and SLS $C_n^2$ scintillometer measurements scaled to 2 m AGL using –4/3 power law. MSA Tower 36A data collected on 30 Oct 21. Data averaging time set at 10 min.**

### 8.2.2 Correlations with Wind Behavior

At day/night transitions, the increase or decline of solar irradiance in the JER region can lead to gradual changes in the wind field due to downslope flow from surrounding elevated terrain or valley flow steering by nearby hills. These phenomena can cause marked fluctuations in $C_n^2$ and in the turbulence inner scale, particularly during stable atmospheric conditions. Figure 30 illustrates a wind direction shift during nighttime stable conditions around 1830 at 2 m AGL on 29 Oct 21 at Tower 36A and approximately 45 min later at 10 m AGL. Both direction shifts were accompanied by increases in wind speed. The earlier transition at the 2-m level apparently indicates a shift from northerly wind direction to a westerly wind direction that mixes slowly upward in the early evening hours. Other, more subtle wind speed and direction shifts at 2 m AGL occur at about 1700 and 2300, respectively.

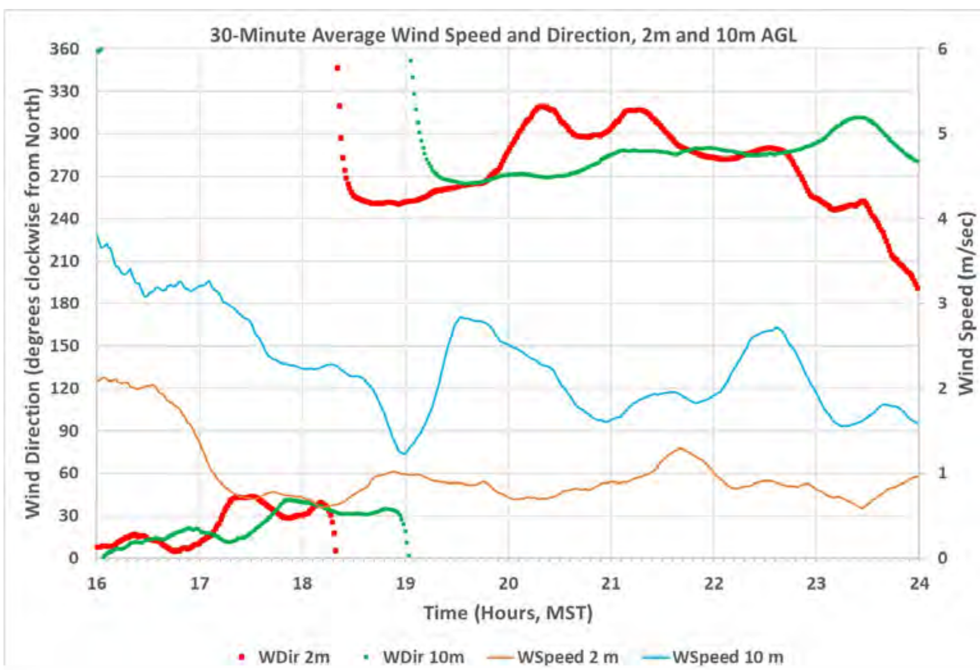


**Fig. 30 Tower 36A evening wind speed and direction at 2 and 10 m AGL, 29 Oct 2021**

Significant correlations of these wind flow events are somewhat apparent in the inner scale and optical turbulence parameters that were measured by the SLS-40A scintillometer, which was located very close to the 2-m AGL height near Tower 36A. Figure 31 is a plot of the inner scale and $C_n^2$ for the same time interval as that of Fig. 30. Approximate times for the evening NE (red line), the drop in 2-m wind speed (yellow line), the first 2-m wind direction shift (green line), and the second 2-

m wind direction shift (blue line) are depicted in Fig. 31. During the hour between the NE and the drop in 2-m wind speed, both the optical turbulence and inner scale increase with relatively little fluctuation. Once the 2-m wind speed drops a few minutes after 1700, both ${C_n}^2$ and the inner scale variability increase markedly, with only slight changes in wind direction. After the wind direction shift around 1830, the inner scale settles to a more stable elevated value, as does ${C_n}^2$. The second, less pronounced, wind direction shift around 2300 shows a lower inner scale and slightly reduced, but still highly variable ${C_n}^2$.

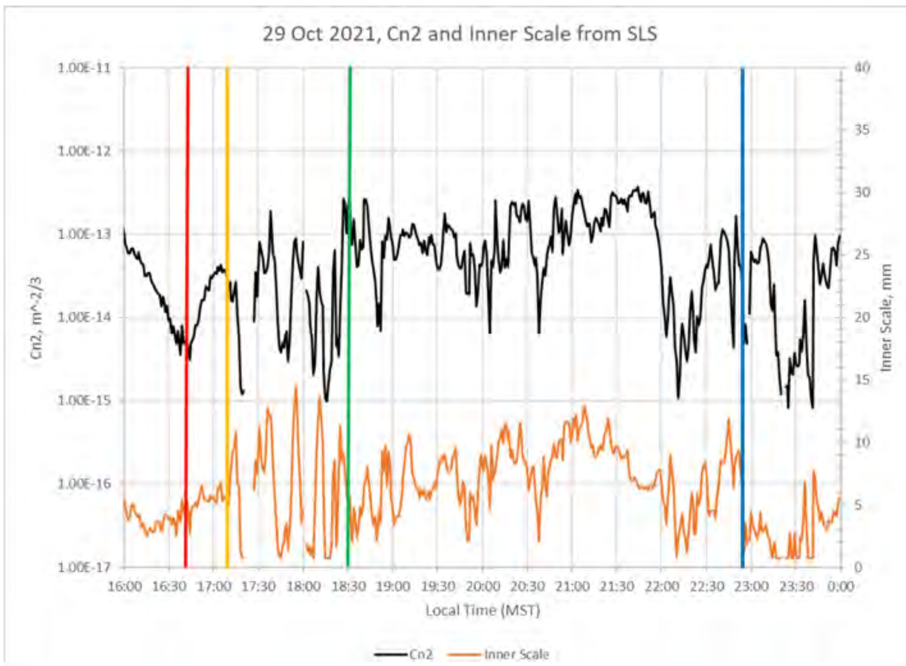


**Fig. 31 SLS ${C_n}^2$ and inner scale, 1600–2400 MST, 29 Oct 2021. Vertical red line indicates approximate NE time, yellow line indicates approximate 2-m AGL wind speed drop time, green line indicates approximate first 2-m AGL wind direction shift time, blue line indicates approximate second 2-m AGL wind direction shift time.**

## 8.3 NAVSLaM-TurbZr Comparisons against Scintillometer Data: NATurE Phase 1

### 8.3.1 Comparison of BLS Scintillometer Measurements with Models

Generally speaking, the BLS scintillometer measurements of ${C_n}^2$ compared well with those derived from the models. Only Tower 36A model results are shown in Figs. 32–34, but other MSA towers displayed similar general agreement during the daytime. One issue with the clear sky results (28, 29, and 30 Oct) is that the model daytime curves display significant variability while the scintillometer curves are much smoother. The 30 Oct NAVSLaM curve has a late afternoon gap in the results due to a numerical issue that remains to be investigated. Nighttime model results usually fell significantly below those of the BLS, sometimes dramatically so. Good temporal correlation between local peaks and troughs in the nighttime model and scintillometer curves was frequently seen, even where the ${C_n}^2$ were in poor agreement. Morning NE minima were indistinct in the most of the model curves, but the evening neutral minimum was usually well resolved by both the model and scintillometer data on both clear and partly cloudy days.

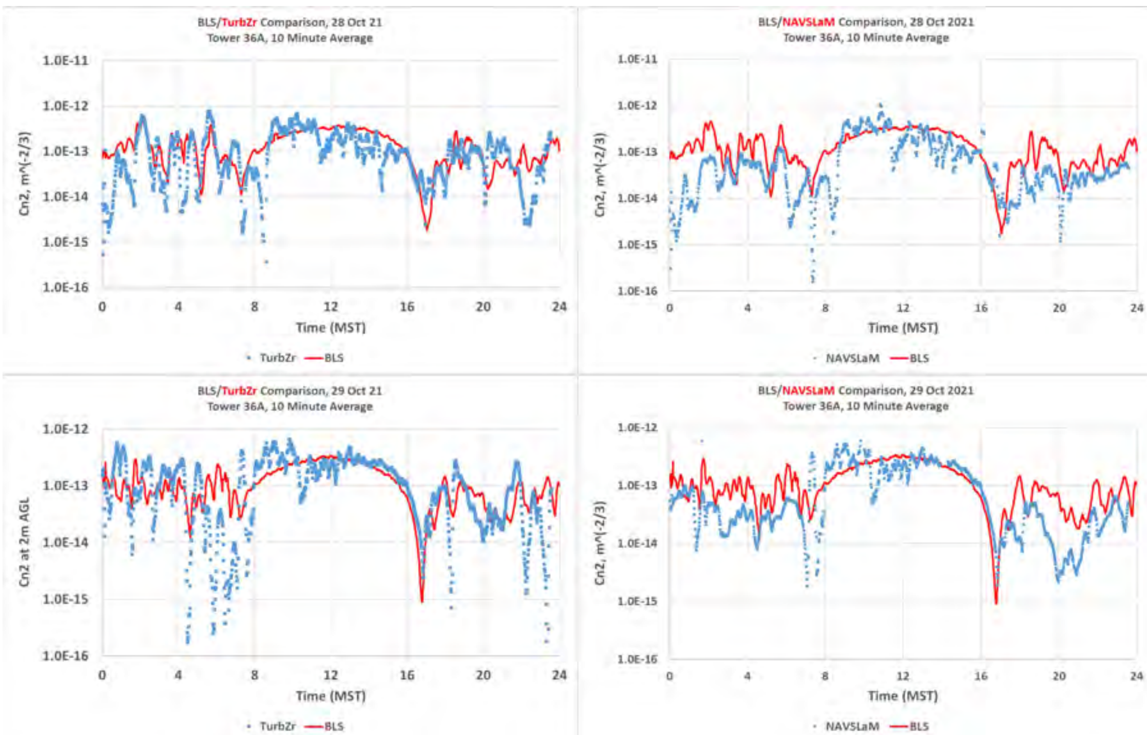


**Fig. 32 Comparison of two-level model predictions of ${C_n}^2$ at 2 m AGL. BLS scintillometer measurements scaled to 2 m AGL using –4/3 power law. MSA Tower 36A data collected on 28 Oct 21 (top row) and 29 Oct 21 (bottom row). Data averaging time set at 10 min.**

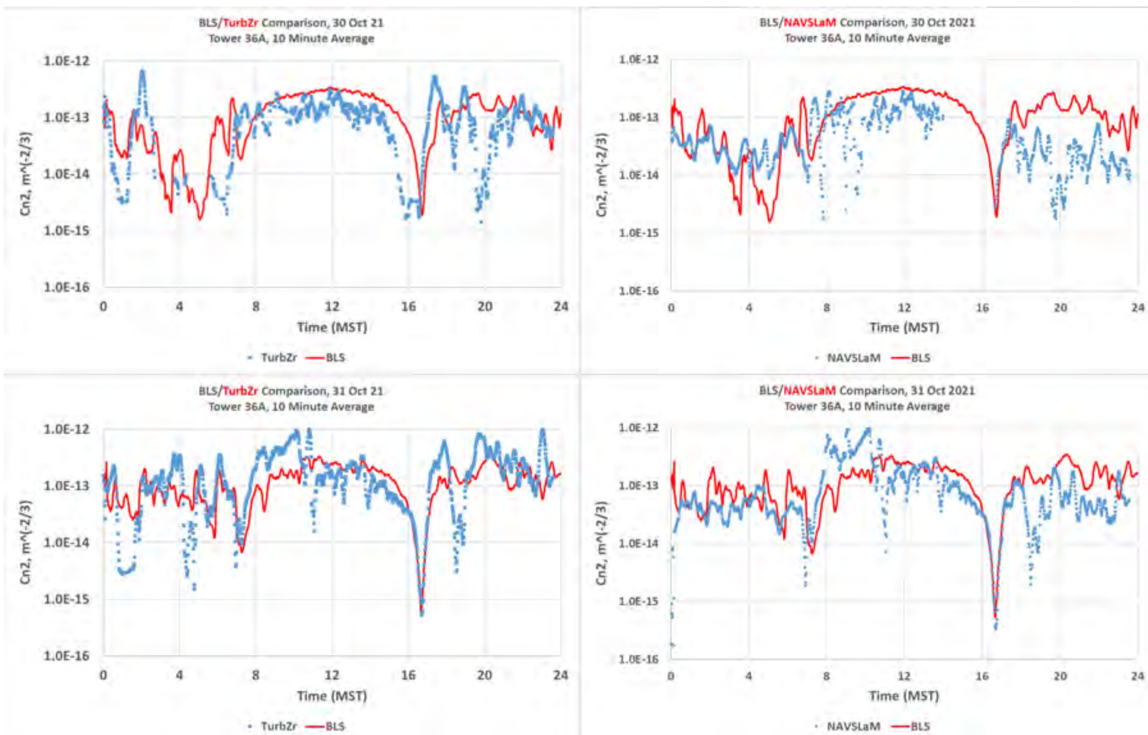


**Fig. 33 Comparison of two-level model predictions of $C_n^2$ at 2 m AGL. BLS scintillometer measurements scaled to 2 m AGL using –4/3 power law. MSA Tower 36A data collected on 30 Oct 21 (top row) and 31 Oct 21 (bottom row). Data averaging time set at 10 min.**

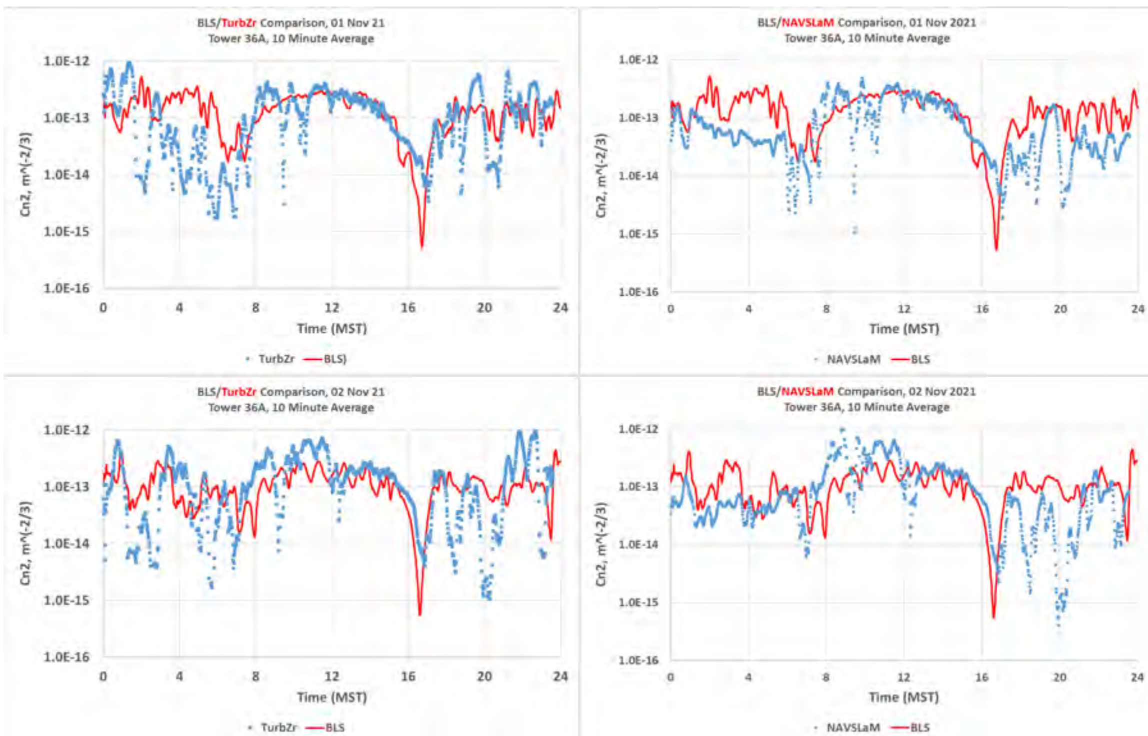


**Fig. 34 Comparison of two-level model predictions of $C_n^2$ at 2 m AGL. BLS scintillometer measurements scaled to 2 m AGL using –4/3 power law. MSA Tower 36A data collected on 1 Nov 21 (top row) and 2 Nov 21 (bottom row). Data averaging time set at 10 min.**

### 8.3.2 Comparison of SLS Scintillometer Measurements with Models

${C_n}^2$ value agreement and temporal correlation between models and SLS data were generally poorer (Figs. 35–37), especially during the daytime hours. Model and SLS dips and peaks frequently did not occur at similar times and were anticorrelated at points. The daytime SLS ${C_n}^2$ values were significantly higher than those predicted by the models in many cases. Nighttime results were inconsistent, with NAVSLaM/SLS agreement sometimes better than that for TurbZr. On many nights, neither model matched well with the SLS results.

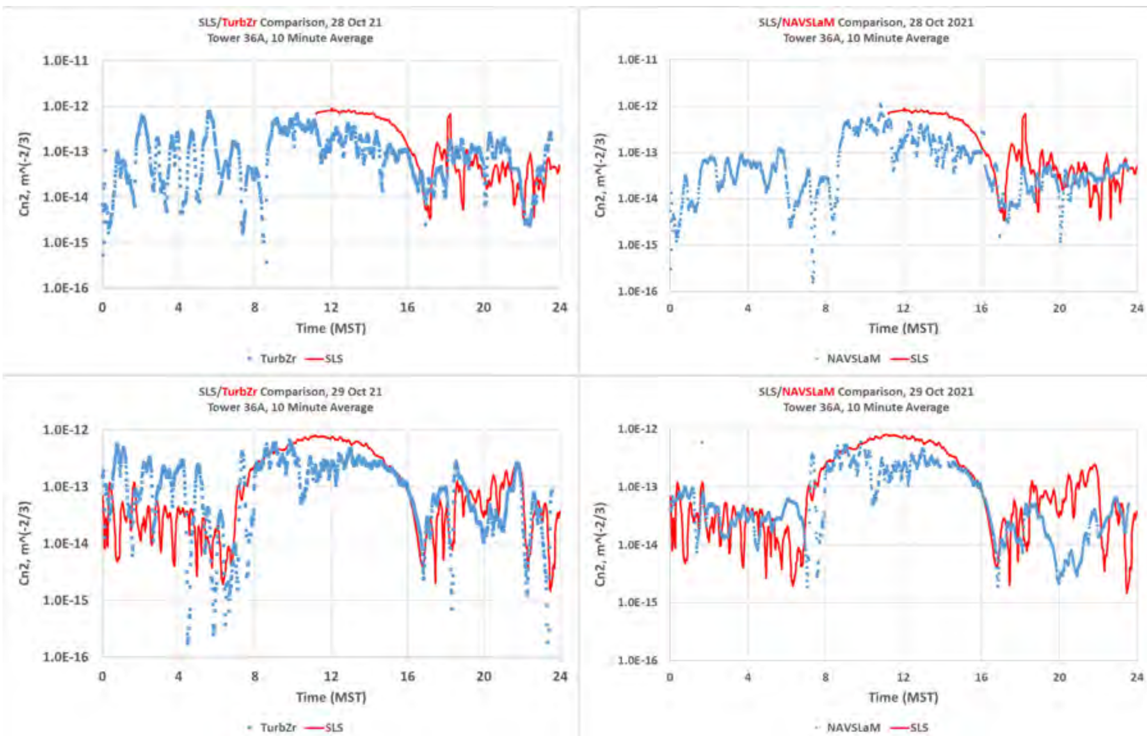


**Fig. 35 Comparison of two-level model predictions of ${C_n}^2$ at 2m AGL. SLS scintillometer measurements scaled to 2 m AGL using –4/3 power law. MSA Tower 36A data collected on 28 Oct 21 (top row) and 29 Oct 21 (bottom row). Data averaging time set at 10 min.**

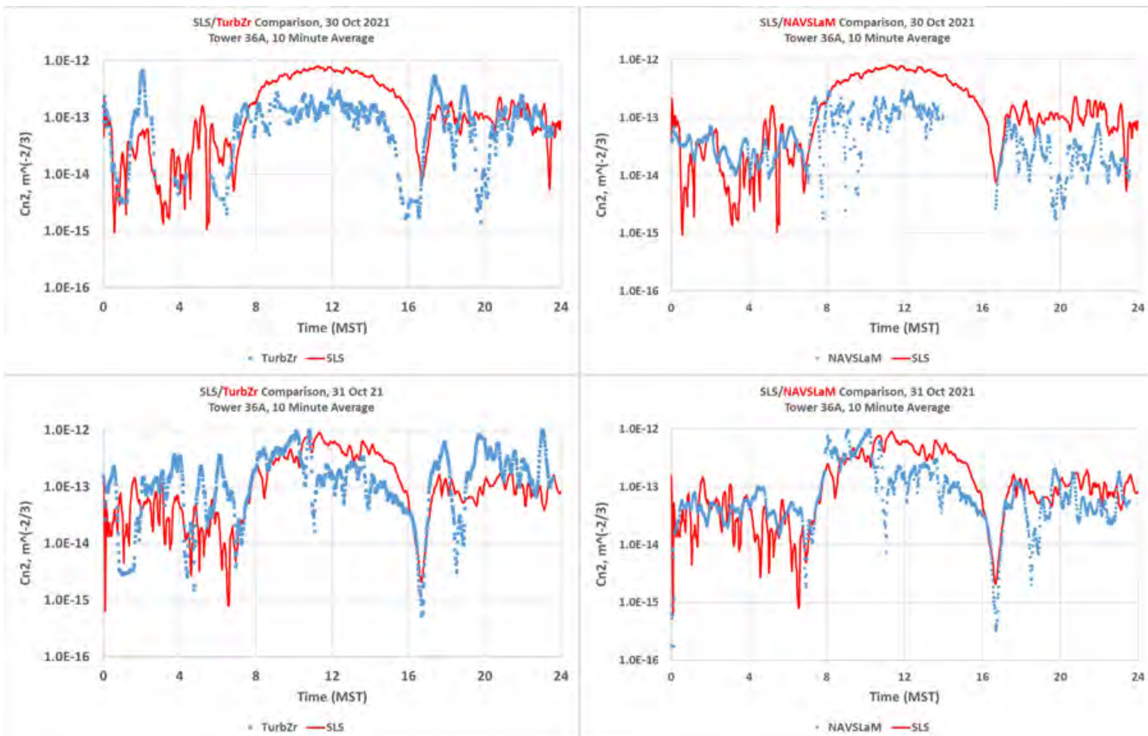


**Fig. 36 Comparison of two-level model predictions of $C_n{}^2$ at 2 m AGL. SLS scintillometer measurements scaled to 2 m AGL using –4/3 power law. MSA Tower 36A data collected on 30 Oct 21 (top row) and 31 Oct 21 (bottom row). Data averaging time set at 10 min.**

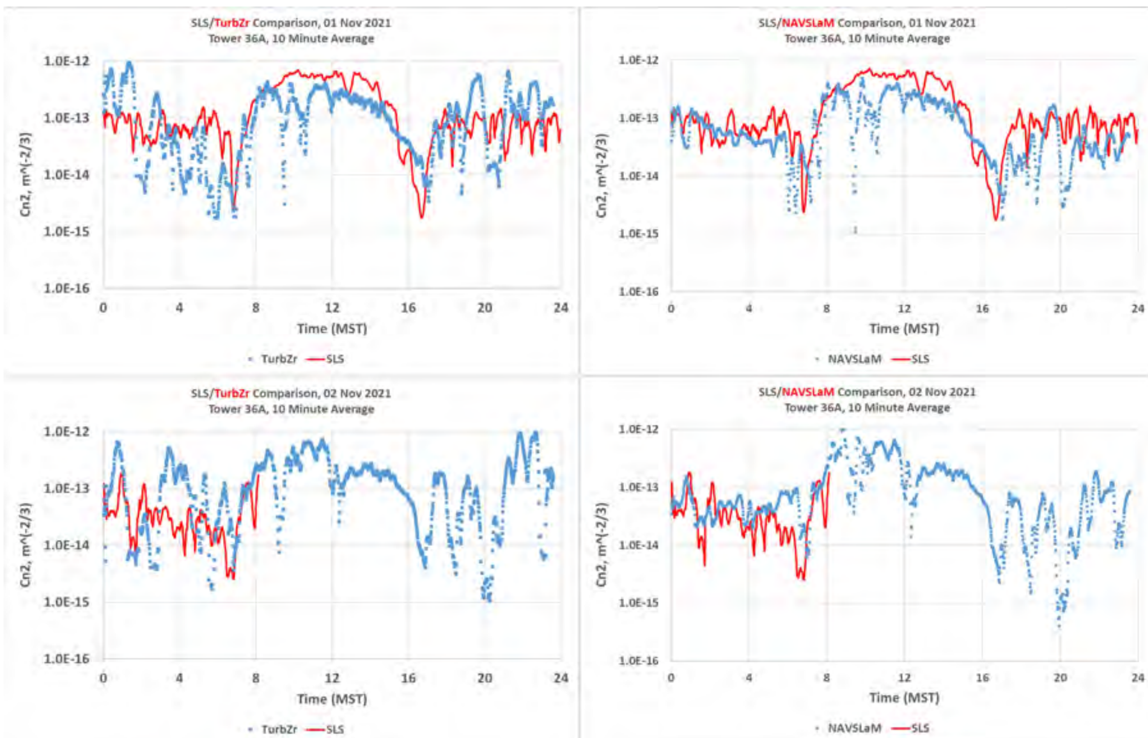


**Fig. 37 Comparison of two-level model predictions of $C_n^2$ at 2 m AGL. SLS scintillometer measurements scaled to 2 m AGL using –4/3 power law. MSA Tower 36A data collected on 1 Nov 21 (top row) and 2 Nov 21 (bottom row). Data averaging time set at 10 min.**

## 8.4 NAVSLaM-TurbZr Comparisons against Scintillometer Data: NATurE Phase 2

The single Phase 2 example day shown in Fig. 38 had only BLS scintillometer data. This day was partly to mostly cloudy. Instead of a focus on Tower 36A, two-level model predictions for all of the fully operational MSA towers (3, 5, 6, 7, and 9–12) are compared with the BLS in its north–south orientation. Interestingly, both models compared well with the scintillometer data for most of the day. TurbZr (Fig. 38) did compare more closely with the scaled BLS during the nighttime hours, however. NAVSLaM (Fig. 39) nocturnal predictions were consistently lower than the BLS at night.

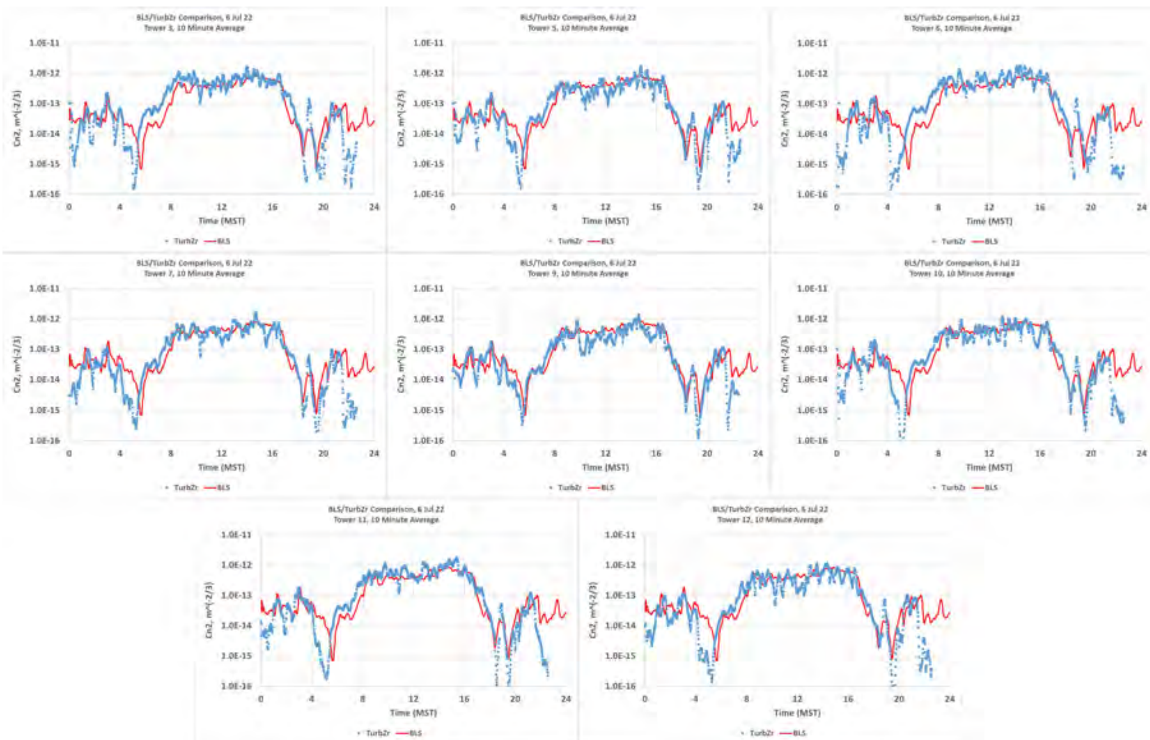


**Fig. 38 Comparison of TurbZr model predictions of $C_n^2$ at 2 m AGL with BLS scintillometer measurements scaled to 2 m AGL using –4/3 power law. MSA Towers 3, 5, 6, 7, and 9–12 data collected on 6 Jul 22. Data averaging time set at 10 min.**

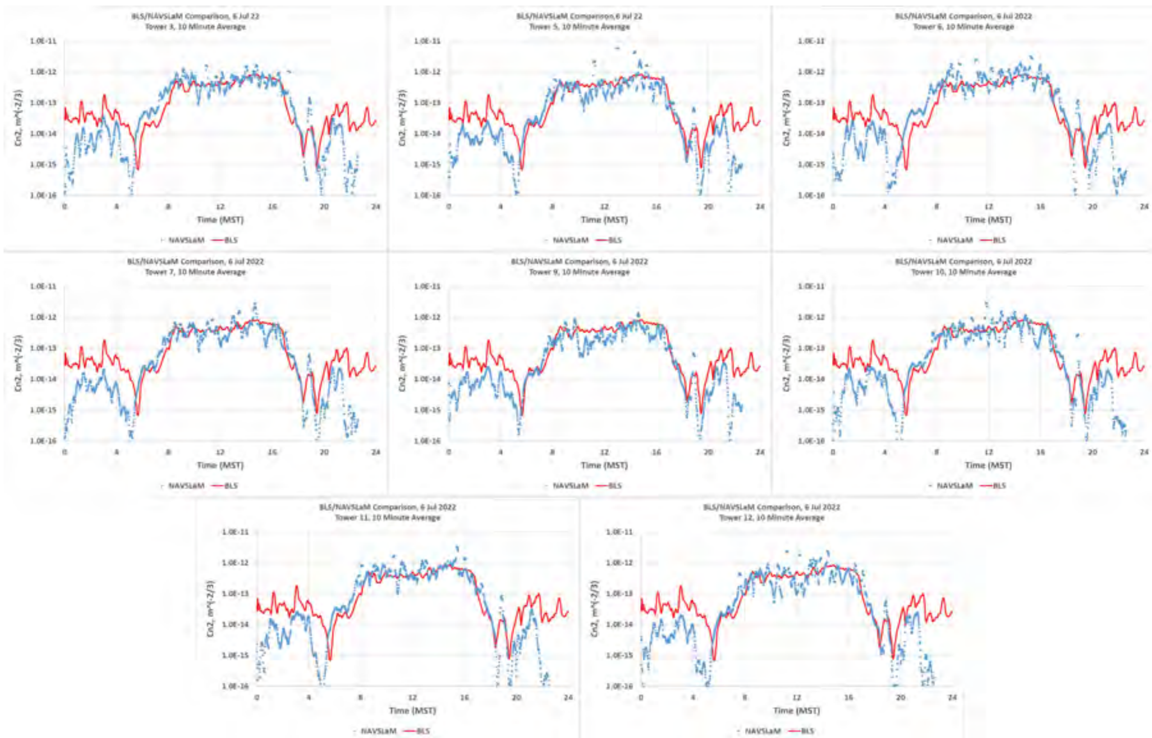


**Fig. 39 Comparison of NAVSLaM model predictions of $C_n^2$ at 2 m AGL with BLS scintillometer measurements scaled to 2 m AGL using –4/3 power law. MSA Towers 3, 5, 6, 7, and 9–12 data collected on 6 Jul 22. Data averaging time set at 10 min.**

## 9. Conclusions

During the daytime (unstable) portion of the day, both the NAVSLaM and TurbZr models compared well with the height-scaled BLS and SLS scintillometer data, particularly for Phase 2 of the NATurE experiment. Stable nocturnal model predictions usually fell below scintillometer observations, although some transient peaks and troughs in the ${C_n}^2$ were tracked by both models, particularly NAVSLaM. TurbZr and NAVSLaM compared well with scaled scintillometer measurements under cloudy conditions that were encountered during the latter part of Phase 1 and the majority of Phase 2. This indicates that the physical models embodied in the codes provide some responsiveness to irradiance-induced surface heat flux variations.

Insight into the horizontal variability of ${C_n}^2$ was provided by comparison of results from various nodes in the MSA tower array for Phase 2. In general, results over the nodal array compared fairly closely in both diurnal level and temporal variation. This has several implications. First, path-averaged measurements (such as those provided by the BLS scintillometer) yield a comprehensive picture of the optical turbulence variation in a desert environment, including transient variations that are induced by surrounding elevated terrain or ambient weather conditions. Second, nodal estimates of ${C_n}^2$ provided by two-level models, sonic anemometers, or other means can feed slant-path tactical directed energy (DE) propagation performance models with reasonable accuracy in a desert environment. Third, the simplicity and passive nature of two-level measurement/model packages makes it feasible to employ them inexpensively and covertly in an operational environment.

However, significant improvements in measurement techniques and analysis details need to made for definitive comparison of the two models with validation data. Apparently, the higher above-ground-level BLS data were cleaner than the SLS data, with less concern about proximity to undulating terrain surfaces that might skew the measurement data. With this in mind, any future experiment might be configured to have multiple two-level meteorological sensor locations along the BLS path, with the BLS path transecting each vertical meteorological sensor stack. Also additional meteorological sensor levels (particularly at 4 m AGL) should be included to get a better estimate of stability conditions.

Overall, the TurbZr model appeared to agree slightly better with the BLS data than did NAVSLaM, although the opposite situation was sometimes seen. Follow-up reports detailing error and correlation analysis results should indicate just how well each model did in an objective fashion. Also, sonic anemometer estimates for ${C_n}^2$ will be added to provide additional estimation of model performance.

## 10. References

1. P. A. Frederickson, K. L. Davidson, C. R. Zeisse, and C. S. Bendall. Estimating the Refractive Index Structure Parameter $(C_n^2)$ over the Ocean Using Bulk Methods. *J. Appl. Meteorol.*, 39:1770–1783, 2000.

2. P. A. Frederickson. Software Design Description for the Navy Atmospheric Vertical Surface Layer Model (NAVSLaM), Version 1.1. Technical report, Naval Postgraduate School, 2015.

3. H. Rachele, A. Tunick, and F. Hansen. MARIAH - A Similarity-Based Method for Determining Wind, Temperature, and Humidity Profile Structure in the Atmospheric Surface Layer. *J. Appl. Meteorol.*, 34:1000–1005, 1995.

4. D. Tofsted, S. O'Brien, and G. Vaucher. An Atmospheric Turbulence Profile Model for Use in Army Wargaming Applications I. Technical Report ARL-TR-3748, US Army Research Laboratory, 2006.

5. S. Barnett, J. Blau, P. Frederickson, and K. Cohn. Measurements and Modeling of Optical Turbulence in the Coastal Environment. *Appl. Sci.*, 12:4892, 2022.

6. E. Aristidi, J. Vernin, E. Fossat, F.-X. Schmider, T. Travouillon, C. Pouzenc, O. Traulle, C. Genthon, A. Agabi, E. Bondoux, Z. Challita, D. Mekarnia, F. Jeanneaux, and G. Bouchez. Monitoring the optical turbulence in the surface layer at Dome C, Antarctica, with sonic anemometers. *MNRAS*, 454:4304–4315, 2015.

# Appendix. Hourly Camera Images

## A.1 Phase 1: 28 Oct 21 - 2 Nov 21

### A.1.1 28 Oct 2021

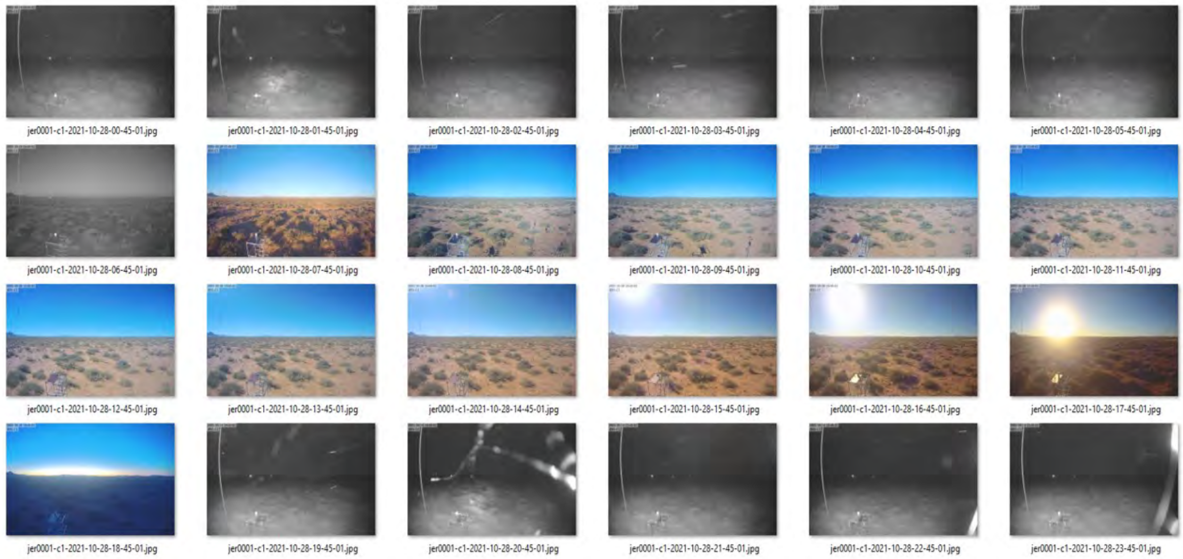


**Fig. A-1 Hourly Tower 1 camera images, 28 Oct 2021**

### A.1.2 29 Oct 2021

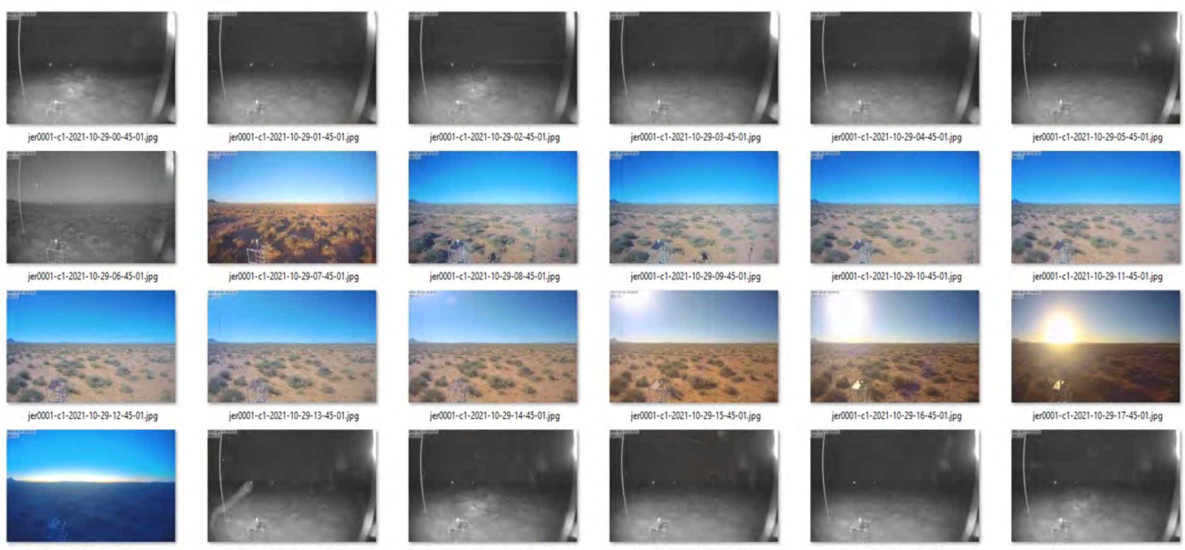


**Fig. A-2 Hourly Tower 1 camera images, 29 Oct 2021**

### A.1.3 30 Oct 2021

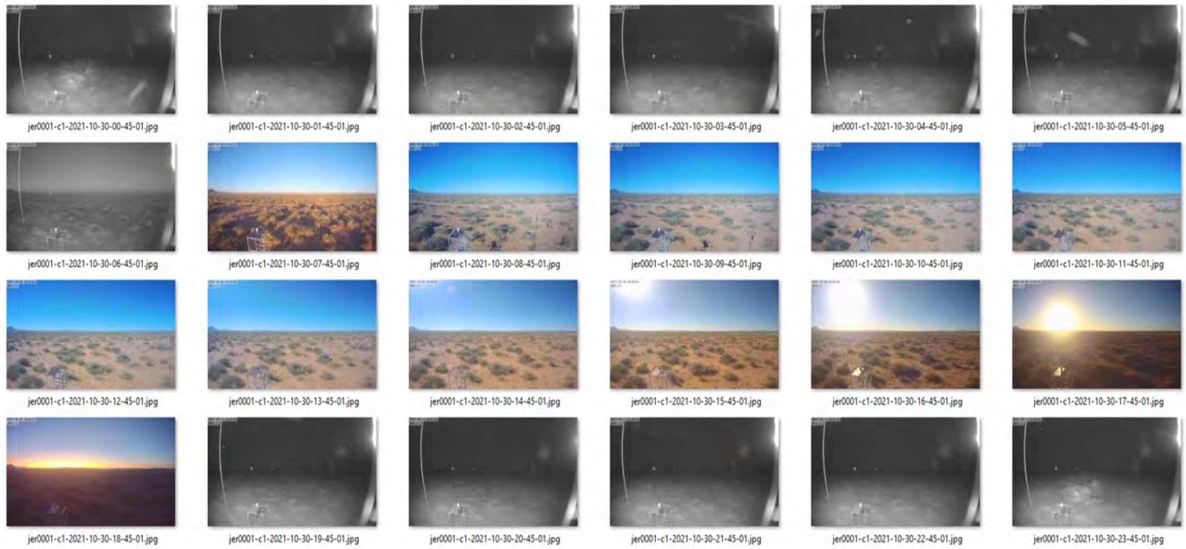


**Fig. A-3 Hourly Tower 1 camera images, 30 Oct 2021**

### A.1.4 31 Oct 2021

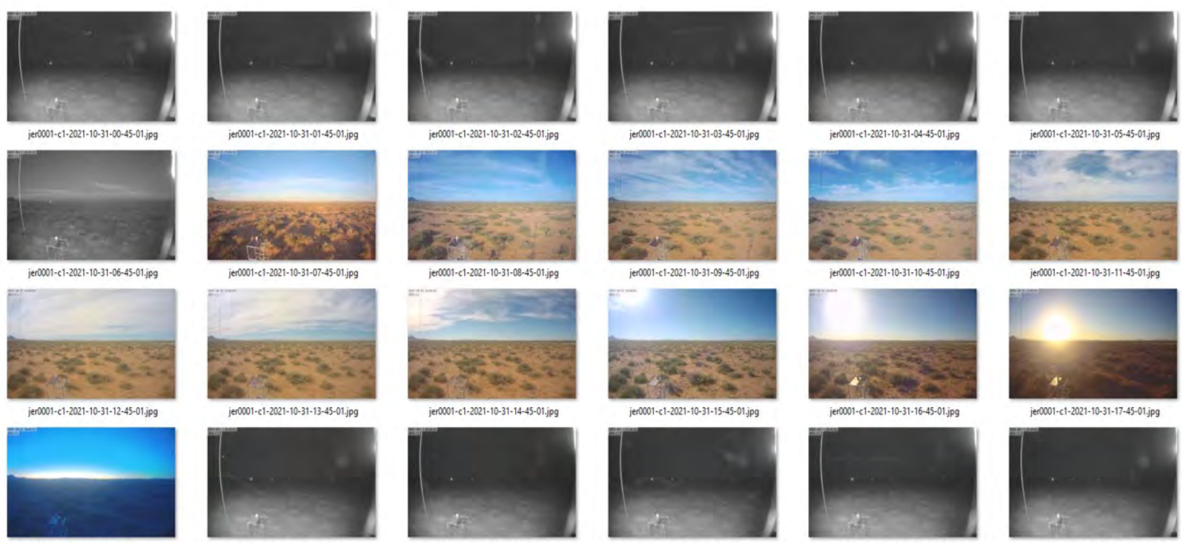


**Fig. A-4 Hourly Tower 1 camera images, 31 Oct 2021**

### A.1.5 1 Nov 2021

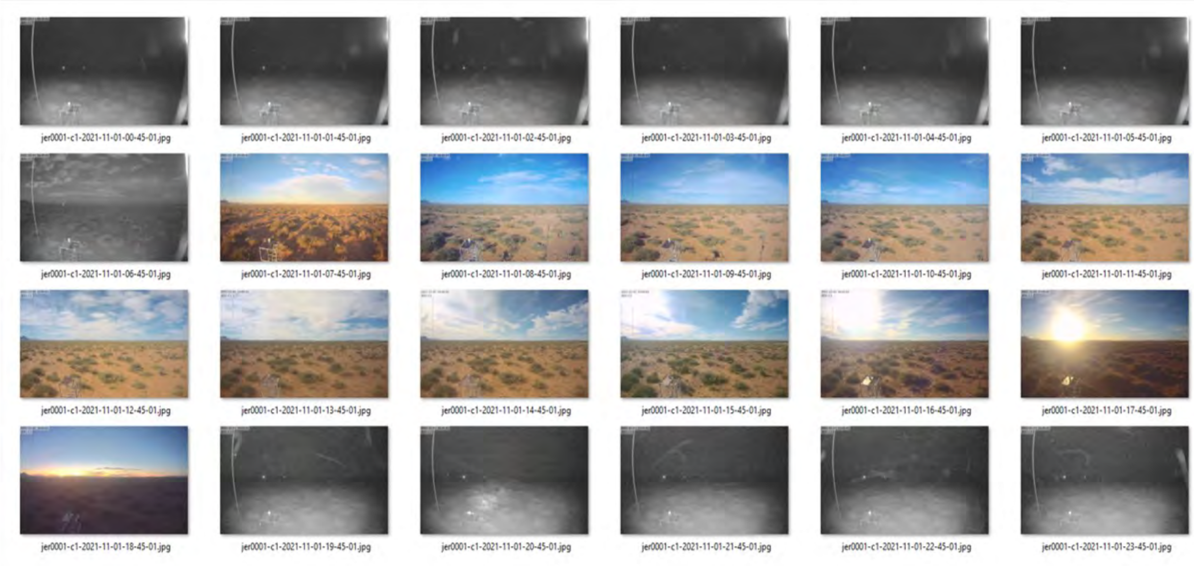


**Fig. A-5 Hourly Tower 1 camera images, 1 Nov 2021**

### A.1.6 2 Nov 2021


**Fig. A-6 Hourly Tower 1 camera images, 2 Nov 2021**

## A.2 Phase 2: 6 Jul 2022

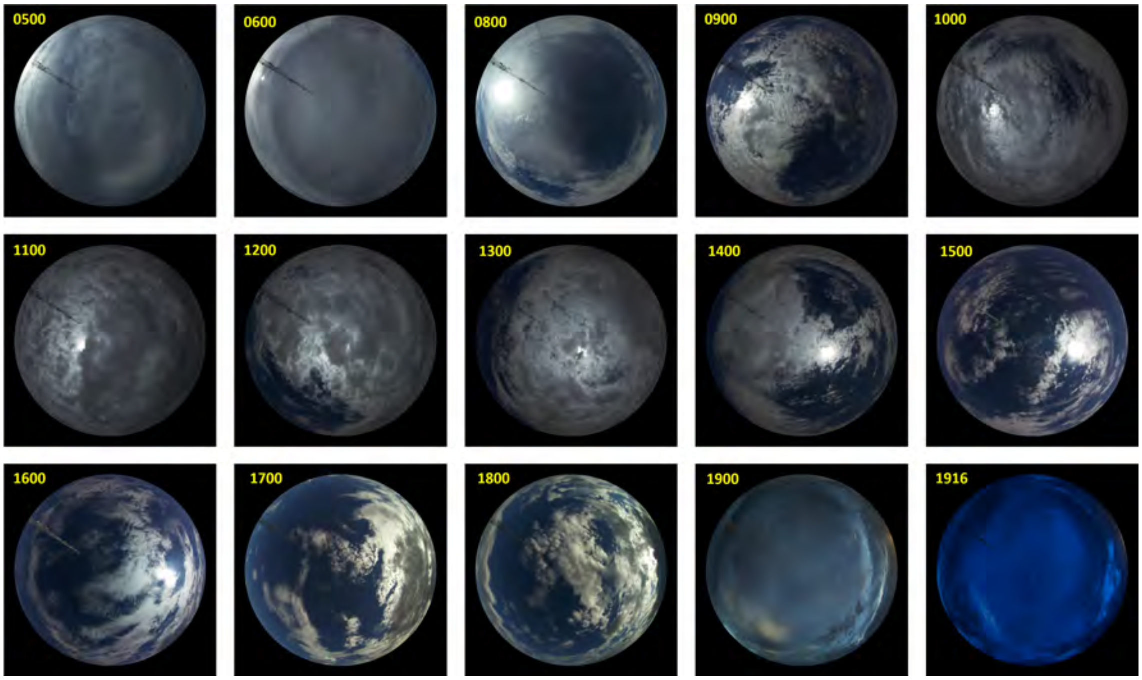


**Fig. A-7 Hourly all-sky camera images, 6 Jul 22**

## List of Symbols, Abbreviations, and Acronyms

| | |
|---|---|
| ARL | Army Research Laboratory |
| ASL | above sea level |
| DE | Directed Energy |
| DEVCOM | US Army Combat Capabilities Development Command |
| DST | Daylight Savings Time |
| JER | Jornada Experimental Range |
| JSON | JavaScript Object Notation |
| MO | Monin–Obukhov |
| MSA | Meteorological Sensor Array |
| MST | Mountain Standard Time |
| NATurE | **NA**VSLaM/**Tur**bZr **E**valuation experiment |
| NAVSLaM | Navy Atmospheric Vertical Surface Layer Model |
| NE | neutral event |
| PC | personal computer |
| TurbZr | Turbulence at Zr model |
| USDA | United States Department of Agriculture |
| UAV | unmanned aerial vehicle |